Computational Study of Manganese, Nitrogen Co-doped Carbon as Electrocatalysts

in Proton Exchange Membrane Fuel Cell

by

Boyang Li

B.S., University of Science and Technology of China, 2017

Submitted to the Graduate Faculty of the

Swanson School of Engineering in partial fulfillment

of the requirements for the degree of

Doctor of Philosophy

University of Pittsburgh

2024

UNIVERSITY OF PITTSBURGH

SWANSON SCHOOL OF ENGINEERING

This dissertation was presented

by

Boyang Li

It was defended on

February 27, 2024

and approved by

Jorg Wiezorek, Ph.D., Professor, Department of Mechanical Engineering and Materials
Science
Wei Xiong, Ph.D., Associate Professor, Department of Mechanical Engineering and
Materials Science
Ian Nettleship, Ph.D., Associate Professor, Department of Mechanical Engineering and
Materials Science
John A. Keith, Ph.D., Professor, Department of Chemical and Petroleum Engineering
Dissertation Director: **Guofeng Wang**, Ph.D., Professor, Department of Mechanical
Engineering and Materials Science

Computational Study of Manganese, Nitrogen Co-doped Carbon as Electrocatalysts in Proton Exchange Membrane Fuel Cell

Boyang Li, PhD

University of Pittsburgh, 2024

Abstract: Renewable energy technologies have been actively pursued in order to meet increasing energy demand and mitigating environmental pollution. Proton exchange membrane fuel cell (PEMFC) is a promising technology with a high energy conversion efficiency to replace the traditional internal combustion engine in automobiles while producing no greenhouse emission. However, the high cost of Pt based electrocatalysts for promoting oxygen reduction reaction (ORR) at the cathode hampers the widespread application of PEMFCs. Showing encouraging performance, non-precious transition metal and nitrogen co-doped carbon electrocatalysts have been extensively developed as cost-effective ORR catalysts in PEMFCs.

This research aims to predict the chemical nature of active sites, kinetic activity for ORR, and structural stability in electrochemical conditions of Mn and N co-doped carbon (denoted as Mn-N-C) catalyst using the first principles density functional theory (DFT) methods. Both D1 type MnN_4 (i.e., a Mn atom coordinated with four pyrrolic N) and D2 type MnN_4 (i.e., a Mn atom coordinated with four pyridinic N) moieties embedded in a carbon graphene layer have been predicted to be active for four-electron ORR in acid media, explaining well available experimental measurement results. Notably, the D1 site was predicted to have a superior limiting potential of 0.80 V for ORR, as compared to the value of 0.54 V on the D2 site, indicating a higher intrinsic ORR activity on the D1 sites. By contrast, the D2 site has been predicted to exhibit enhanced electrochemical stability over the D1 site, as evidenced by the predictions that the free energy

change for demetallation process is 0.36 eV higher for the D2 site than the D1 site. Moreover, a constant potential computational method combined with a microkinetic model for ORR has been developed and applied to predict the half-wave potential of ORR to be 0.73 V on D2 site, agreeing well with experimental values to validate the developed computational approach. Motivated by the predicted stability of two types of MnN_4 sites, the free energy evolution along a transformation pathway from D1 to D2 site has been computed to examine novel synthesis concept for enhancing the electrochemical stability of Mn-N-C catalysts.

Keyword: proton exchange membrane fuel cell, oxygen reduction reaction, non-precious metal catalyst, density functional theory, adsorption energy, activation energy, nudged elastic band, microkinetic model, solvation model

Table of Contents

List of Tables

List of Figures

x

Preface

The pursuit of a PhD is an extensive journey filled with numerous challenges, encompassing moments of success and failure, gain and loss, joy and frustration. I cannot get through this journey without those people who supported me, assisted me, and guided me.

Foremost, my heartfelt gratitude goes to my PhD advisor, Prof. Guofeng Wang. I am very fortunate to have been under his mentorship. His patience, profound knowledge, and consistent encouragement have been pivotal in my pursuit of PhD. His guidance, instruction, and inspiration have profoundly influenced me and will continue to be of immense value in my future.

I owe much appreciation to my committee members, Prof. Jorg Wiezorek, Prof. Ian Nettleship, Prof. Wei Xiong, and Prof. John Keith, for their valuable insights and critiques of my research work. Additionally, my thanks go to my group members—Dr. Kexi Liu, Dr. Zhenliu Liu, Dr. Weitao Shan, Siming Zhang, and Ying Fang—for their support throughout this work.

I must also express my profound appreciation to my experimental collaborators—Prof. Gang Wu, Dr. Yuyan Shao, Prof. Liangbing Hu, and Prof. Chao Wang. Their concerted efforts were indispensable in achieving our research results.

Last but not least, my deepest thanks to my parents for their unwavering and unconditional love and support.

1.0 Introduction

With the development of science and technology, the energy demand is increasing annually. According to the data from U.S. Energy Information Administration, the usage of fossil fuels, including coal, natural gas and petroleum, takes 79% of the total energy consumed in U.S[1]. Regarding that the fossil fuels are a non-renewable energy and their combustion results in greenhouse emissions like CO_2, it is essential to develop renewable energy with efficient energy conversion efficiency. The transportation sector, which accounts for 24% of total energy consumption in U.S[1], primarily depends on fossil fuels. Currently, the majority of vehicles are powered by internal combustion engine (ICE). However, ICE suffered from the relatively low electrical efficiency, ranging from 20 to 40%, and considerable exhaust emissions. In comparison, fuel cell technology shows a significantly higher energy conversion efficiency up to 60% and emits less pollution (**Figure 1.1**). Therefore, fuel cell technology presents a compelling alternative to ICE for automotive power generation, combining enhanced efficiency with environmental benefits.
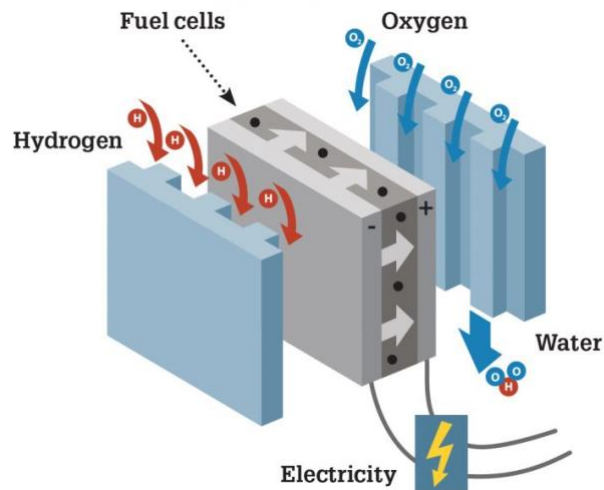
Figure 1.1 Scheme of H_2-O_2 fuel cell

Fuel cells are capable of converting the chemical energy from fuel into electrical energy. Generally, they are categorized by the electrolyte they employ and the temperature range in which the cell operates (**Figure 1.2**). The solid oxide fuel cell (SOFC) and molten carbonate fuel cell (MCFC) are operated at high temperature over 600 ℃, which have been used in many practical applications. Alkaline fuel cell (AFC) is the first developed fuel cell technology which were used as power systems in the U.S space program[2]. The Phosphoric acid fuel cell (PAFC) is one the most mature fuel cell and first used in commerce. The proton exchange membrane fuel cell (PEMFC) delivers a high power density with operating at low temperature[3]. Among these fuel cells, the PEMFC is particularly advantageous for transportation applications and the development of PEMFC has become new direction for future automotive power solutions, offering a promising alternative to traditional power sources.
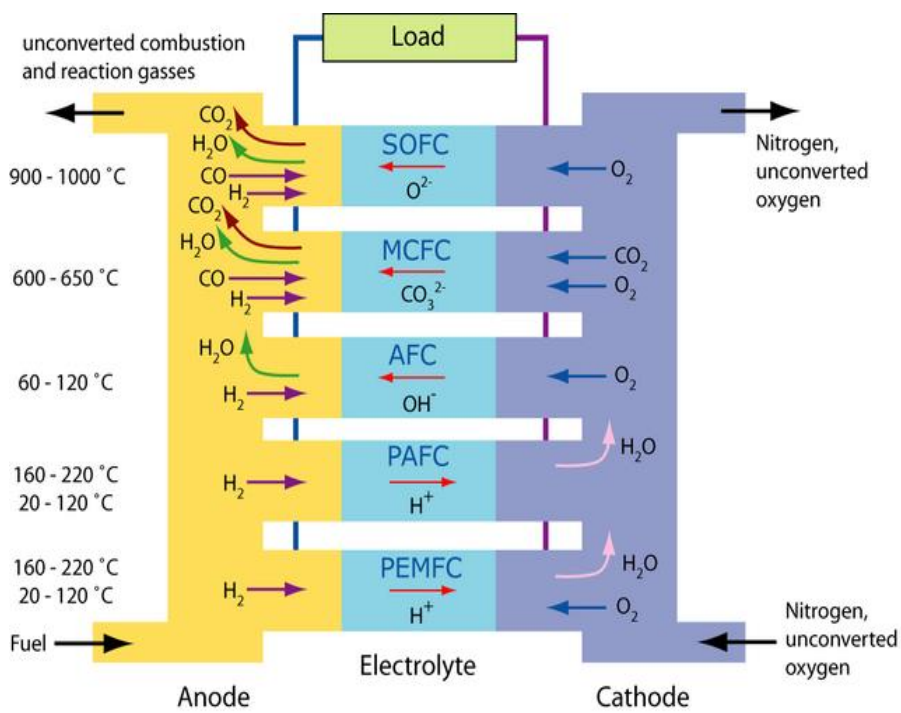
Figure 1.2 Scheme of SOFC, MCFC, AFC, PAFC, and PEMFC.

The PEMFC consists of anode, cathode, and proton exchange membrane. On the anode, the hydrogen gas is decomposed to form protons and electrons. Meanwhile, the oxygen gas on the cathode would react with the protons penetrating from proton exchange membrane and electrons transferring from external circuit, to form water. The anode and cathode reactions are termed as hydrogen oxidation reaction (HOR) and oxygen reduction reaction (ORR), respectively. Due to the relatively low operating temperature for PEMFC, both electrode reactions are kinetically sluggish, especially ORR and hence a highly efficient catalyst is necessary for PEMFC. Currently, the platinum group metal (PGM) catalyst is considered as the most efficient catalyst for ORR[4]. However, the scarcity and high cost of PGM hinder the propagation of PEMFC. Data from General Motors[5] suggest that reducing the Pt loading in PEMFC to $0.0625mg/cm^2$ while achieving a power density above $1.0 \ W/cm^2$ is essential for the widespread implementation of PEMFC. Consequently, research is now focusing on two main strategies: reducing Pt loading and developing PGM-free alternatives (**Figure 1.3**). To improve the mass efficiency of Pt in PGM catalyst, many studies have been reported, such as synthesizing Pt nanoparticles[6,7], Pt-based alloy[6,8-10], or introducing carbon support into PGM catalyst[10,11]. However, the discovery of PGM-free catalyst to replace Pt is necessary in a long-term consideration.
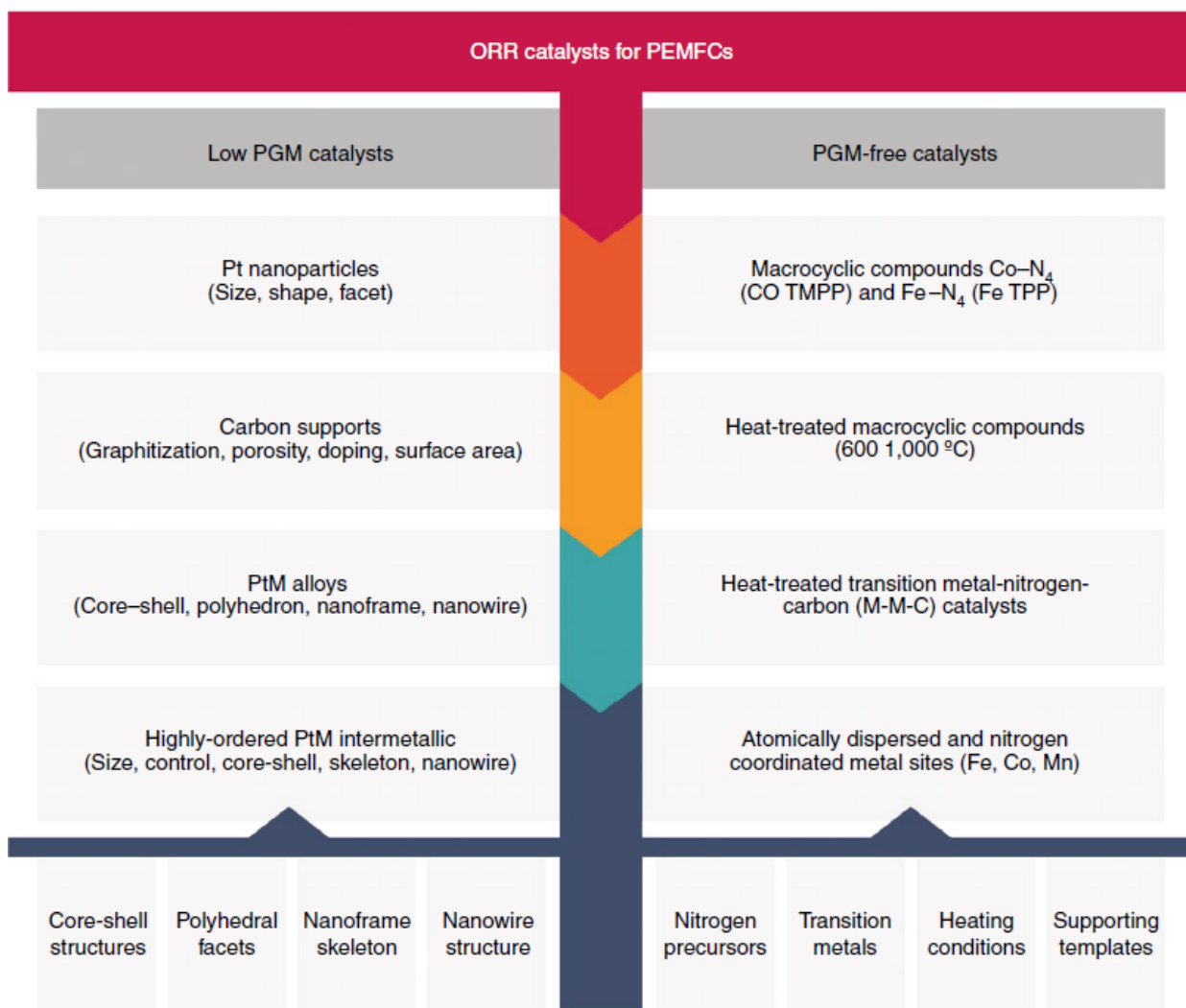
Figure 1.3 Development of cathode catalysts for PEMFCs. Low-platinum group metal (PGM) and PGM-free catalyst approaches are currently explored for near- and long-term applications for transportation, respectively.[12]

In last several decades, the development of non-precious transition metal and nitrogen co-doped carbon (TM-N-C) materials as ORR catalyst made a huge progress. In the 1960s, macrocyclic compounds like metal phthalocyanine were first reported to exhibit ORR activity[13]. Subsequently, the high temperature pyrolysis method was developed to enhance the ORR activity and stability for these macrocyclic-compound derived catalyst[14-16]. Over the last two decades, it

was widely reported that the TM-N-C catalysts exhibited a high ORR activity, which is comparable to that of PGM catalyst[17-19]. These TM-N-C materials are typically synthesized via pyrolyzing mixture containing transition metal salt, nitrogen precursor and carbon materials at a temperature over 700 °C. Among these studied transition metals, the Fe-N-C material was reported as the most promising ORR catalyst[18,19], followed by Co-N-C[20] and Mn-N-C[21]. However, TM-N-C catalysts suffer from low active site density and insufficient stability during ORR, which limit their application in PEMFC. The activity loss may ascribe to the dissolution of metal active site, carbon corrosion, carbon oxidation, and micropore flooding[22]. Specifically, the Fe-N-C catalyst are criticized by participating in the Fenton reactions, in which the dissolved Fe ions react with H_2O_2, a byproduct from the 2e⁻ ORR pathway[23]. Consequently, the OH radical generated from Fenton reaction would degrade the membrane and shorten the lifetime of PEMFC. In addition, Co-N-C catalyst struggle with a high selectivity to H_2O_2, leading to the degradation of catalyst via carbon oxidation[24]. Unlike Fe and Co, Mn-N-C catalysts are not involved in Fenton reaction and their high selectivity to 4e⁻ pathway also inhibits the generation of H_2O_2. In a recent study, Mn-N-C catalyst was reported to show a high ORR activity with a half-wave potential ($E_{1/2}$) of 0.80 V and a promising stability of 17 mV loss after 30,000 cycles[21]. Hence, it is of significance to identify the active site and understand how it works in Mn-N-C catalyst.

Complementing experimental efforts, the first-principles density function calculation is essential to gain insight into the underlying mechanism of catalysis. It has been turned out that combining theory and experiment is significantly powerful in heterogeneous catalyst investigating and design in many electrochemical processes, such as CO_2 reduction, nitrogen reduction, oxygen evolution and oxygen reduction reaction.[25-28]

In this dissertation, intensive DFT calculations have been performed to elucidate the chemical nature of active sites, kinetic activity of ORR and catalyst stability on Mn-N-C (and Fe-N-C catalyst as reference). Specifically, two type of MnN_4 active sites including porphyrin-like D1 site and fully embedded D2 site with various local coordination environment have been identified. The intrinsic ORR activity and stability of these two active sites have been thoroughly examined. Moreover, in-depth electronic structure analysis has been carried out to shed light on the reason behind the promising ORR activity and stability exhibited by these two active sites. The dissertation also explores strategies to enhance the ORR activity and stability inherent to these sites, like introducing S or H near active sites. Moreover, a constant potential computational method combined with a microkinetic model has been developed and applied to predict polarization curve of ORR. As a result, many studies have been made to explore Mn-N-C catalyst, significantly expanding the scientific understanding of its role in promoting ORR.

2.0 Background

2.1 Experimental Investigation of TM-N-C Catalyst for ORR

2.1.1 Synthesis of TM-N-C Catalyst

Traditional TM-N-C catalyst synthesis approach is via high temperature (> 700ºC) treatment of the mixed transition metal precursor, nitrogen source and carbon-based support[29-32]. Generally, the metal salt like chlorates and macrocyclic complex like Fe polyacrylonitrile are used as metal precursor[19]. Nitrogen source includes nitrogen-containing molecules like phenylenediamine and NH_3 gas[33]. The latter is generally introduced in heat treatment step. The carbon-based support contains graphene, carbon nanotube (CNT)[34,35], carbon nanofiber (CNF)[36,37], which could provide a good electronic conductivity. All precursors are mixed via ball-milling or wet-impregnation method[37] and then are pyrolyzed under N_2, Ar/H_2, or NH_3 environment at temperature over 700 ºC.[38] In general, the temperature over 700 ºC could enable all carbon graphitized to keep a high electronic conductivity, whereas the primary pyrolyzed product at temperature below 500 ºC consists of polymer and carbon nitride.[39,40] Finally, the acid leaching is adopted to etch some inactive metal (like metal cluster) and other impurities, yielding TM-N-C catalyst with a partially graphitized microporous carbon.[19,41]

The ORR activity of TM-N-C catalyst is optimized via changing the type of precursor, synthesis parameter (such as heat treatment temperature, heat treatment duration, the loading ratio between different precursors), and synthesis procedure. For example, Wu and co-workers synthesized a series of Fe-N-C catalyst using $FeCl_3$ as Fe precursor, pyrrole as nitrogen precursor

and carbon nanofibers as carbon-based support under different temperature (from 600 to 1000 ℃) and different ratio of FeCl$_3$/pyrrole.[30] They found that the ORR activity of Fe-N-C catalyst highly depended on the synthesis parameters. In other work, Li et.al synthesized an atomically dispersed Mn-N-C catalyst via two-step synthesis method involving doping and adsorption process.[21] The second doping step significantly enhances the ORR activity and stability through effectively increasing the active site density.

The catalysts synthesized by these methods always show a highly heterogeneous morphology, including multiple carbon phases and disordered element distribution.[19] The mess of catalyst hinders our understanding to the real active site for ORR. Consequently, how to design an optimal precursor including TM, N and C with a uniform mixing at atomic level is inevitable to further gain insight into TM-N-C catalyst. In last decade, metal organic framework (MOF) emerged as a promising precursor for TM-N-C, owing to its pre-existed M-N-C bond and porous structure[42-44]. The synthesized Fe-N-C catalyst using ZIF-8 precursor exhibited a promising ORR performance especially the power density measured in membrane-electrode assemblies (MEAs).[45,46] In the synthesis process, Fe ions could partially replace Zn ions in tetrahedral Zn–N$_4$ complexes in ZIF-8 to form a Fe-N$_4$ complexes and then these Fe-N4 complexes were converted in-situ into FeN$_4$ active sites during thermal activation, providing atomic-level dispersion of Fe active sites. [45] Due to the relatively boiling temperature of Zn (907 ℃), the heat treatment results in the evaporation of Zn and thus creates highly porous morphologies, providing high specific area and active site density.[47] The retained polyhedral morphology from ZIF-8 also inhibits the growth of metal participle. The atomically dispersed Fe-N-C catalyst derived from ZIF-8 exhibited a significantly enhanced ORR activity in acid media ($E_{1/2}$ of 0.86 V versus the reversible hydrogen

electrode), with a current density of 0.044 A cm^{-2} at 0.89 V (0.029 A cm^{-2} at 0.9 VIR-free) in a

MEA test (H$_2$–O$_2$ at 1.0 bar).[12]

     Figure 2.1a shows the development of PGM-free catalyst over last 15 years. In 2008, Lee et.al synthesized Fe-N-C catalyst via pyrolyzing FeSO$_4$, ethylene diamine and carbon black. The obtained catalyst exhibited a half wave potential of 0.72 V, indicating that Fe-N-C catalyst is active to promote ORR.[48] In 2011, the reported half wave potential of synthesized Fe-N-C catalyst increased to 0.80 V, comparable with that of 0.86 V of commercial Pt/C.[19] In 2018, Wu and co-workers further improved the half wave of atomically dispersed Fe-N-C to 0.87 V, slightly higher than commercial Pt/C catalyst.[49] Recently, Zeng et.al reported a Fe-ion-doped ZIF-8 derived catalyst pyrolyzed at forming gas which shows remarkable half-wave potential of 0.896 V, indicating that Fe-N-C catalyst shows an encouraging prospect to replace Pt-based catalyst.[50] Besides the Fe-N-C catalyst, the Co-N-C[20,51] and Mn-N-C[21,52] catalyst also exhibited promising ORR activity, however the intrinsic activity and the density of atomically dispersed active sites still require to further improve to reach the level of practical application. In addition, doping other heterogenous atom such as B, S and P, was reported as a new strategy to improve the intrinsic ORR activity[53-55]. For example, Guo et.al found that S doped Mn-N-C catalyst exhibited encouraging ORR activity with a $E_{1/2}$ of 0.810 V in acid media, higher than that of Mn-N-C catalyst with $E_{1/2}$ of 0.776V.[54] The S doping could modify the electronic structure near MnN$_4$ site, and thus improve the intrinsic ORR activity. **Figures 2.1b** and **2.1c** summarize the ORR performance of M-N-C catalysts in $E_{1/2}$ and MEA fuel cell power density, respectively. The difference in $E_{1/2}$ between TM-N-C and commercial Pt/C catalysts was only several millivolts in electrochemical test, but the performance of TM-N-C catalysts still falls far from that of commercial Pt/C in real MEA test. Although encouraging activity and stability improvements for TM-N-C catalyst in last

9

two decades, PGM-free catalyst still could not reach the DOE activity target of >0.044 A cm^{-2} at

0.9 VIR-free in MEAs.[49]
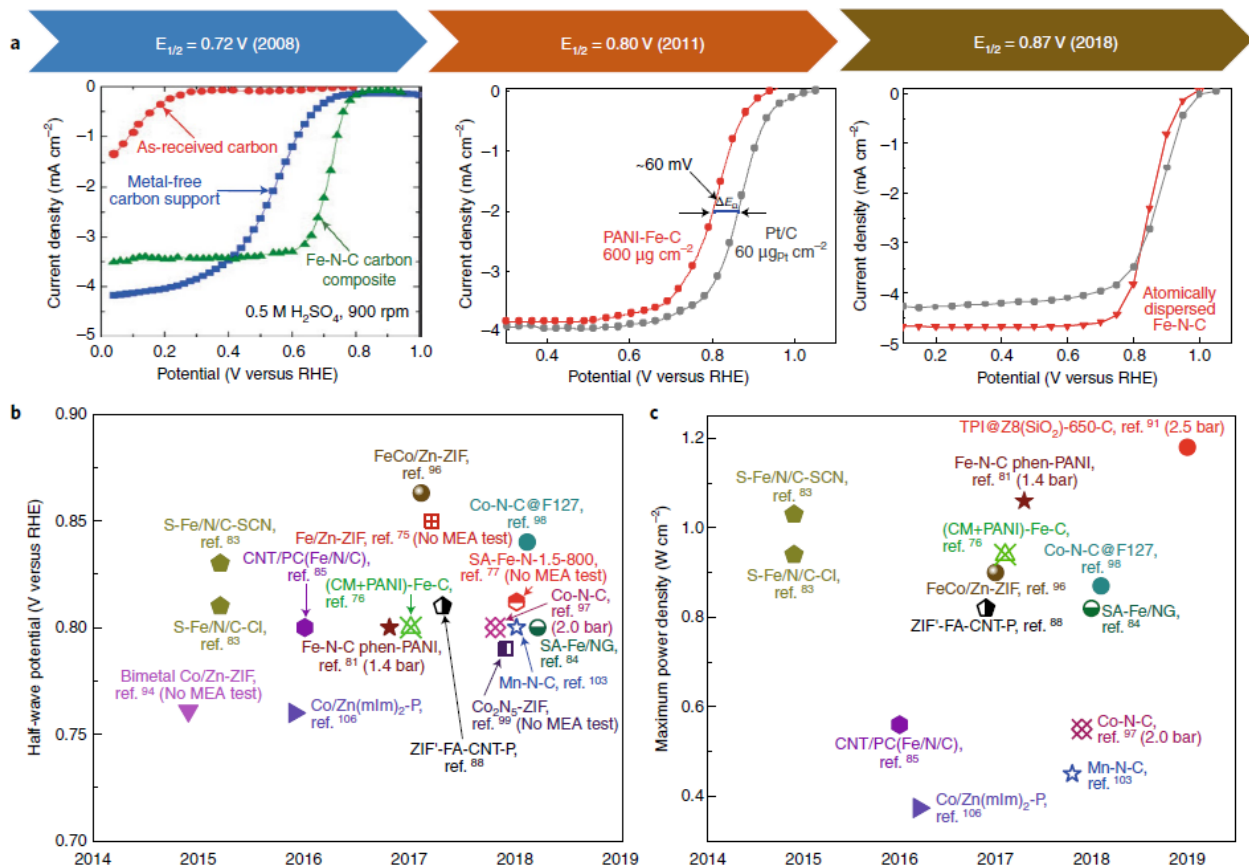
Figure 2.1 Significant ORR activity enhancement for Fe-N-C catalysts from 2008 to 2018 with a positive shift of

half-wave potential over 100 mV. b, Measured half-wave potential of various M-N-C catalysts in acidic media. c,

The reported maximum power density in PEMFCs using TM-N-C as ORR catalysts under H$_2$–O$_2$ conditions at

temperature of 80 °C.[12]

2.1.2 Characterization of TM-N-C

The development of catalyst characterization techniques such as high-resolution transmission electron microscopy, X-ray adsorption spectroscopy and Mössbauer spectroscopy, is important to identify the ORR active site in TM-N-C catalyst. Transmission electron microscopy (TEM) is recognized as the most direct technique to observe the element distribution in materials. In 2017, Hoon et.al utilized high-resolution transmission microscopy, high-angle annular dark-field scanning transmission electron microscopy, and aberration-corrected scanning transmission electron microscopy to study the element distribution in Fe-N-C catalyst and found that Fe atoms were atomically dispersed in Fe-N-C catalyst. Electron energy-loss spectroscopy (EELS) result further turned out that Fe atom was coordinated with N atoms, suggesting the presence of Fe-N_x moiety in Fe-N-C catalyst.[56-58] However, it is still a challenge to directly obtain the coordination number between TM and N using electron microscopic technique due to the highly heterogenous structure of TM-N-C catalyst.[59,60]

In last decade, X-ray adsorption spectroscopy, including X-ray absorption near edge structure (XANES) and extended X-ray adsorption fine structure (EXAFS), as a highly sensitive technique to determine local coordination environment, played an important role in revealing the nature of the active site in TM-N-C[61-64]. For example, Zitolo et al. found that the signal of Fe-Fe bond was absent in EXAFS, suggesting that Fe atoms are atomically dispersed in Fe-N-C[62]. The coordination environment of Fe in Fe-N-C catalyst was identified as FeN_4 with a Fe-N bond ranging from 1.90 to 2.01 Å. This result was accomplished via comparing the K-edge XANES measured in experiment and theoretical spectrum calculated with the possible potential structures.

However, the X-ray adsorption spectroscopy has its limitations to provide detailed information about the local structure surrounding the TM-N$_4$ site.

^{57}Fe Mössbauer spectroscopy is another powerful technique to identify Fe species with different electronic state. Through this technique, Jaouen and co-workers identified two distinct Fe sites within Fe-N-C catalyst: the high-spin FeN$_4$C$_{12}$ site and the low- or intermediate-spin FeN$_4$C$_{10}$ site. These two sites assigned to FeN$_4$ moieties but embedded in different ways in the carbon substrate[65,66]. Moreover, in situ ^{57}Fe Mössbauer spectroscopy revealed that high-spin FeN$_4$C$_{12}$ site exhibits greater ORR activity but less stability than the low- or intermediate-spin FeN$_4$C$_{10}$ site. It should be mentioned that the Mössbauer spectroscopy technique is specific to Fe-N-C material and cannot be applied to identify active sites in Co-N-C or Mn-N-C materials. Nevertheless, there is a belief that if the synthesis process for Mn-N-C and Fe-N-C (or Co-N-C) materials are same, the structure of the active sites should be analogous.

2.1.3 Electrochemical Measurement

To assess the performance of ORR catalyst, there are several important properties including kinetic activity for ORR, catalyst stability and selectivity between two-electron pathway and four-electron pathway. These properties are measured by electrochemical test or membrane electrode assemblies (MEA) tests. The electrochemical test works on the three electrodes system (**Figure 2.2**), including a working electrode (WE), a counter electrode (CE), and a reference electrode (RE). The catalysts are loaded onto the WE, where the ORR occurs. The WE and CE form a circuit, while the RE works as a stable potential reference electrode, unaffected by variations in conditions

like pH and temperature. For enhancing the diffusion of O_2 during ORR electrochemical test, the WE is typically required to rotate, known as the rotating disk electrode (RDE) technique.

The ORR activity in electrochemical test is evaluated using half-wave potential, defined as a potential at which the measured current is equal to a half of diffusion current. A catalyst exhibiting a higher half-wave potential is indicative of superior ORR activity. Another key indicator for ORR activity is the volumetric current density, which is measured at a specific potential (commonly 0.8 V or 0.9 V) on the polarization curve. A higher current density at this potential correlates with enhanced ORR activity.

The stability of TM-N-C catalyst is usually examined by long term stability test.[67-69] This test method compared the ORR activity before and after multiple potential cycles and the difference between them is used to evaluate the ORR stability. Alternatively, holding at constant potential or constant current density for a long time such as 0.8 V or 0.9 V is another approach to assess the stability of TM-N-C materials.[21]

During the oxygen reduction to water (4e$^-$ pathway), the oxygen could also be reduced to hydrogen peroxide through 2e$^-$ pathway. The H_2O_2 is an active molecule which may result in the carbon oxidation in TM-N-C materials or Fenton reaction in Fe-N-C catalyst[70]. Moreover, the 2e$^-$ pathway also shows a lower energy efficiency as compared to 4e$^-$ pathway. Therefore, the ORR selectivity is crucial to assess the performance of ORR catalyst. The pathway selectivity can be determined via Koutecky-Levich equation using RDE method[71] . The Koutecky-Levich equation is:

$$\frac{1}{j} = \frac{1}{j_k} + \frac{1}{0.62nFD_O^{2/3}v^{-1/6}C_{O_2}w^{1/2}} \tag{2-1}$$

where n is the number of electrons transferred, F is the Faraday constant, D_{O2} is the diffusion coefficient of oxygen, v is the viscosity of the solution, C_{O2} is the bulk oxygen

concentration, and w is the electrode rotating speed. The current density j and rotating speed w can be obtained in experiment, other parameters including F, D_{O2}, v and C_{O2} are constant under a given condition. Consequently, the transferred electron number can be calculated via fitting current density j and rotating speed w. Other approach to measure the electron transferred number is via rotating ring disk electrode (RRDE), in which the current density on ring could directly represent the hydrogen dioxide yield. The H_2O_2 yield can be calculated via equation below.

$$Y_{H_2O_2} = \frac{2j_{ring}}{N*j_{disk}+j_{ring}}$$
(2-2)

where N is the collection efficiency, j_{ring} is the current density of ring and j_{disk} is the current density of disk.
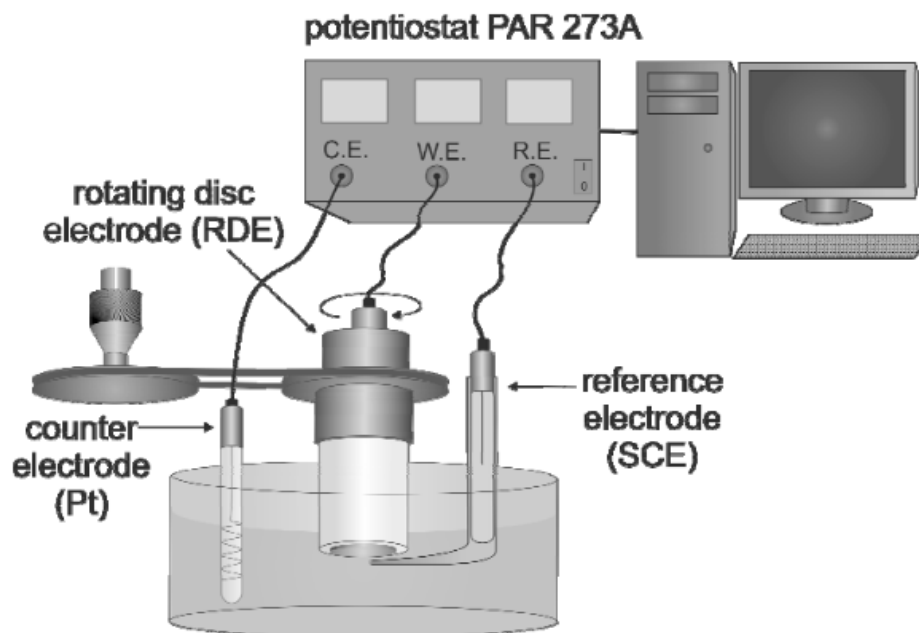
Figure 2.2 Scheme of the electrochemical workstation with three electrode system

2.2 Oxygen Reduction Reaction (ORR) Mechanism

In PEMFC, the general process of oxygen reduction reaction can be proceeded by four-electron pathway as shown in **eq.2-3**

$$O_2 + 4H^+ + 4e^- \rightarrow 2H_2O \qquad\qquad E_0 = 1.23\,V \qquad\qquad \textbf{(2-3)}$$

Meanwhile, the partial reduction of oxygen may occur via **eq.2-4** as a by-reaction.

$$O_2 + 2H^+ + 2e^- \rightarrow H_2O_2 \qquad\qquad E_0 = 0.70V \qquad\qquad \textbf{(2-4)}$$

It should be mentioned that both of **eq.3** and **eq.4** are proton-coupled electron transfer (PCET) reaction. Protons and electrons are obtained from electrolyte and electrode, respectively. The standard electrode potential of **eq.3** and **eq.4** are 1.23 V and 0.70 V, respectively, suggesting the reduction of oxygen being exothermic. Depending on the catalyst, both of the two-electron and four-electron ORR pathways could occur (**Figure 2.3**). The two-electron pathway as shown in **eq.2-5** initiates from the adsorption of O_2 molecule on catalyst surface, then the adsorbed O_2 is protonated to form adsorbed OOH and free H_2O_2, sequentially. It should be noted that the two-electron partial oxygen reduction is a by-reaction in PEMFC due to its relatively low power density. In comparison, the fully reduced four-electron pathway involving in four elementary steps is more complicated. Regrading whether the O_2 dissociates before protonation, there are two types of four-electron pathway, namely, associative pathway and dissociative pathway. Following associative four-electron pathway (**eq.2-6**), O_2 molecule will first adsorb on the catalyst surface, and then O_2 will be reduced to form *OOH, *O, *OH and H_2O, sequentially. Here, the asterisk represents the molecule adsorbed on catalyst surface. In contrast, the O_2 will first dissociate to form two adsorbed O, then protonated to form *OH and H_2O along dissociative pathway (**eq.2-7**).
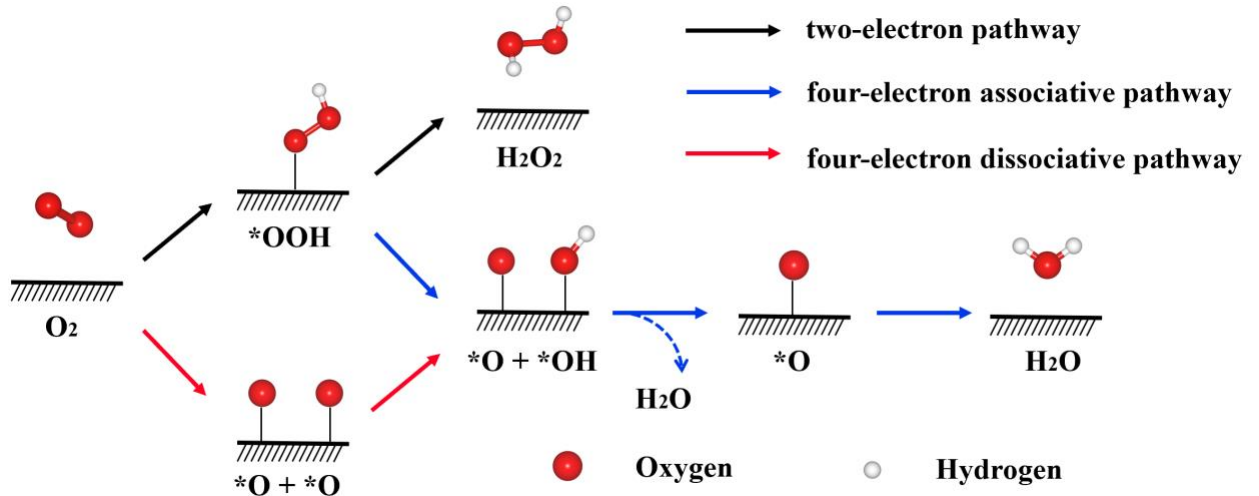
Figure 2.3 Scheme of ORR two-electron, four-electron pathway

$$O_2 + 2H^+ + 2e^- \rightarrow * OOH + H^+ + e^- \rightarrow H_2O_2 \tag{2-5}$$

$$O_2 + 4H^+ + 4e^- \rightarrow * OOH + 3H^+ + 3e^- \rightarrow * O + * OH + 3H^+ + 3e^- \rightarrow * O +$$

$$2H^+ + 2e^- + H_2O \rightarrow * OH + 3H^+ + 3e^- + H_2O \rightarrow 2H_2O \tag{2-6}$$

$$O_2 + 4H^+ + 4e^- \rightarrow 2 * O + 4H^+ + 4e^- \rightarrow * O + * OH + 3H^+ + 3e^- \rightarrow * O +$$

$$2H^+ + 2e^- + H_2O \rightarrow * OH + 3H^+ + 3e^- + H_2O \rightarrow 2H_2O \tag{2-7}$$
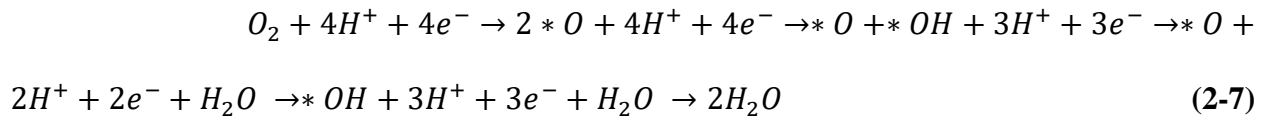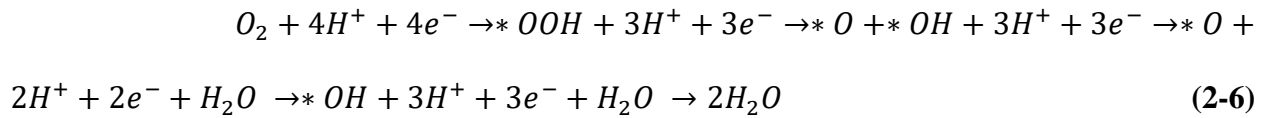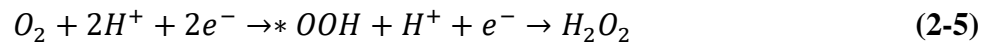
To reveal the thermodynamics of ORR, it is essential to ascertain the free energies of ORR intermediate including O_2, *OOH, *O, *OH, and H_2O, along with the proton−electron pair. The free energies of these species can be determined from DFT calculation, and the free energy of proton−electron pair is calculated using computational hydrogen electrode (CHE) model[72]. In CHE model, the free energy of a single proton−electron pair is defined as −eU relative to H_2 in

the gas phase at standard conditions, where U is the electrode potential with respect to the reversible hydrogen electrode (RHE). Based on these results, we could draw an ORR free energy evolution which illustrates the free energy change of each elementary step of ORR.

Figure 2.4a depicts a free energy evolution of four-electron associative ORR pathway on Pt (111).[73] At U=0V, all the free energy steps are downhill, suggesting ORR being thermodynamically feasible at this potential. In contrast, at the potential of 1.23V, i.e., equilibrium potential for four-electron pathway, the transition from OH to H_2O exhibits an uphill free energy step, suggesting that Pt (111) surfaces would be covered by OH, thereby impeding the ORR. The highest potential where all of free energy steps become downhill is defined as the limiting potential. For Pt(111), this limiting potential is predicted to be 0.8V.[73] A higher calculated limiting potential represents a higher predicted ORR activity. It should be noted that the definition of limiting potential aligns closely with the experimentally measured onset potential, which is the potential where the ORR current density begins to increase sharply. This approach could also be applied to two-electron pathway as demonstrated in **Figure 2.4b**. The limiting potential of two-electron pathway on $PtHg_4$ is calculated to be 0.64 V.[74]
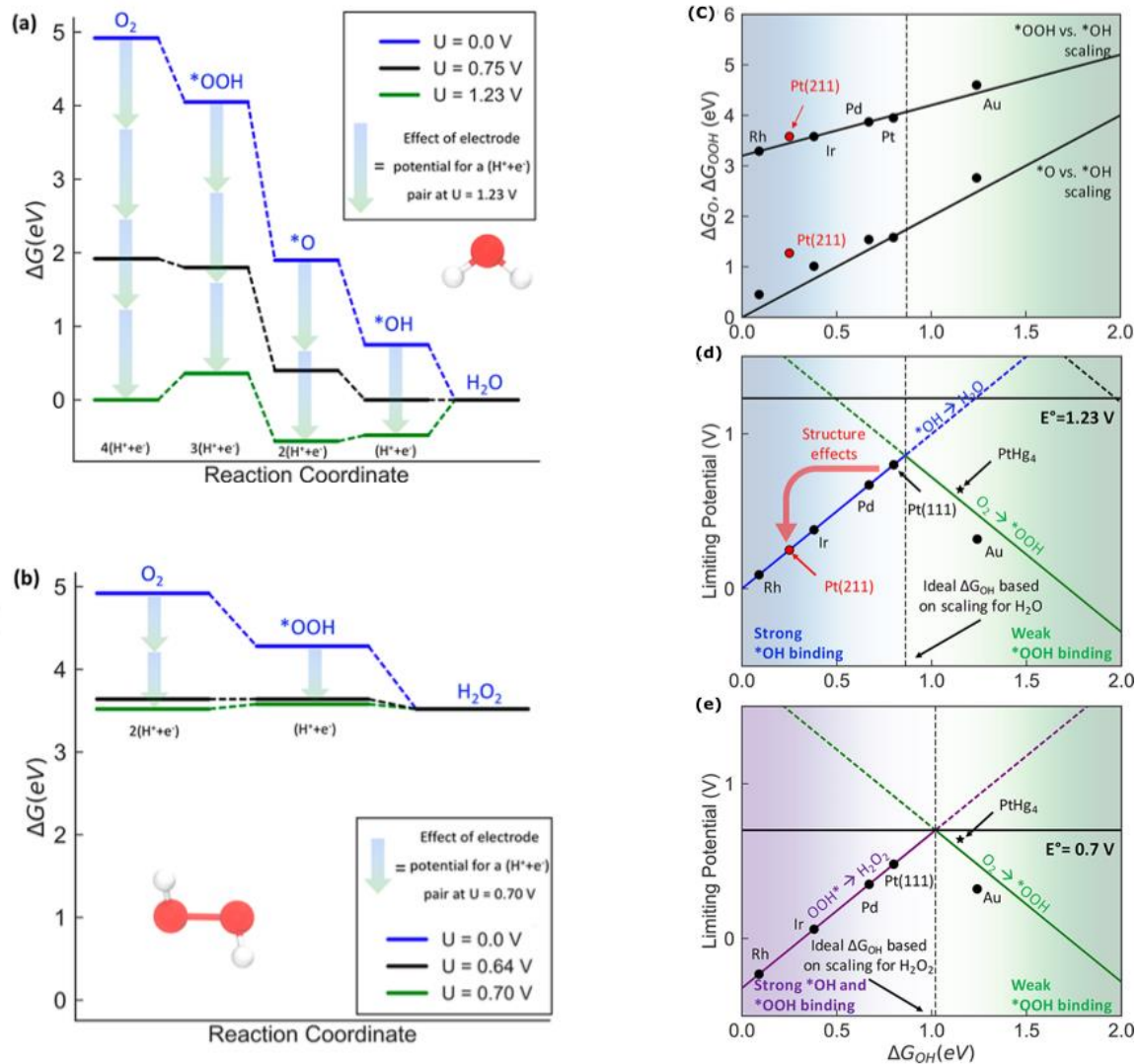
Figure 2.4 (a) Free energy evolution for ORR on Pt(111) via four-electron associative pathway and (b) on PtHg$_4$ via two-electron pathway. (c) Scaling relation for the chemisorption energies of *OOH and *O for the (111) surface of various metals (black circles) using *OH as a descriptor. (d) The relation between limit potential of four-electron pathway and chemisorption of *OH. (e) The relation between limit potential of two-electron pathway and chemisorption of *OH. The Figure(a) and (b) are shown under three different potentials: 0 V (blue lines), the corresponding equilibrium potential (green lines), and the limiting potential (black lines). [75]

Kulkarni et al. discovered a significant scaling relationship between the chemisorption energies of *OH and those of *OOH or *O, as shown in **Figure 2.4c**.[75] This finding suggests that

the chemisorption energies of *O and *OOH are linearly dependent on the chemisorption energy of *OH. As a result, the theoretical limiting potential for the ORR can be predicted based on the free energy of *OH, and the graphical representation of this relationship is commonly referred to as a volcano plot. In **Figure 2.4d**, the solid blue line depicts the region where *OH is strongly bound, while the solid green line represents the region of weakly bound *OOH. The peak of volcano represents the maximum ORR activity with an optimal chemisorption of OH. The point corresponding to Pt(111) is close to the peak of volcano, explaining the encouraging ORR activity for PGM catalyst. Similar volcano plot for two-electron reduction is shown in **Figure 2.4e**.[75]

The kinetics of the ORR are essential for a deeper understanding of ORR activity. As illustrated in **Figure 2.5**, thermodynamics alone would predict the four-electron pathway to be more favorable than the two-electron pathway on Au(111). However, this prediction is not in line with experimental observations that the two-electron pathway is more favorable on Au (111) surfaces. To resolve this inconsistency, kinetic activation energies for both the OOH dissociation and the reduction of OOH to H_2O_2 were calculated.[76] The kinetic analysis reveals that the OOH dissociation reaction has a higher energy barrier, which accounts for the suppressed four-electron pathway on Au (111). Generally, such kinetic calculations can predict the selectivity between the two-electron and four-electron pathways, providing a more comprehensive picture that integrates both thermodynamic favorability and kinetic accessibility.
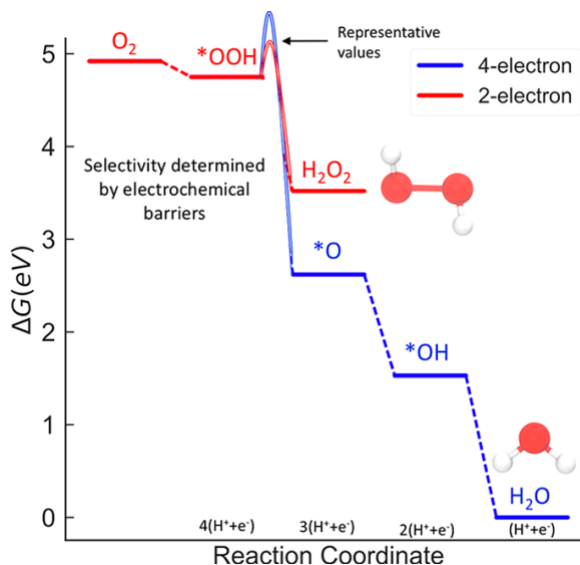
Figure 2.5 Free energy diagram for the four- and two-electron oxygen reduction on Au(111).[75]

2.3 Computational Investigation of TM-N-C Catalyst for ORR

In the study of TM-N-C for ORR, the DFT calculations were adopted to complement experiment in two aspects. One is to identify the active sites for ORR via screening the ORR activity of multiple possible sites, the other aspect is to gain insight of how ORR occurs on these active sites. Hobly and co-workers investigated multiple possible FeN_x sites (x=2-4) on the edge of graphene layer[56]. They found that FeN_3 and FeN_4 structures are stable, whereas FeN_2 structure are not, via calculating formation energy. In other work, Zhong et al. calculated the adsorption of H_2O on FeN_x sites (x = 1-5) and pointed out that FeN_1, FeN_2 and FeN_3 sites bind H_2O so strongly that the produced water cannot desorb from active site and move to electrolyte.[77] Liu et.al performed DFT calculations to study the $4e^-$ ORR mechanism on three types of FeN_4 site with different local carbon structure.[78] In this study, three FeN_4 sites were predicted to be active for

20

ORR and the FeN_4C_8 site with FeN_4 moiety bridging adjacent zigzag graphitic edges was proposed as the most active FeN_4 site among them. Zeng et al. conducted a series of DFT calculations on $TM-N_4$ and $TM-C_4$ sites with considering 11 types of transition metals.[79] They found a good linear relation between the free energy of *OH and *OOH, and this predicted relation was close to that on metal surface. Moreover, they proposed a new universe descriptor to evaluate catalytic activity.

In the other aspect, many studies investigated the ORR mechanism on $TM-N_4$ site. Liu et.al predicted the activation energy of OOH dissociation step to be 0.56 eV on FeN_4 site and 1.11 eV on CoN_4 site, respectively[80]. This result indicates that OOH dissociation could proceed on FeN_4 site, but is not favorable on CoN_4 site, explaining the low selectivity to H_2O on Co-N-C catalyst. Zhao and co-workers adopted ab initio molecular dynamics (AIMD) to compare activation energy between O-O dissociation and Co-O dissociation, and pointed out Co-O bond being more stable than O-O bond.[81] The microkinetic model is another powerful tool to correlate the experiment and DFT calculations. Specifically, the microkinetic model involves in multiple elementary steps, such as diffusion, adsorption, desorption, and surface reaction. The reaction rate could be calculated from the pre-factors, concentration of reactant species, and activation energy. Consequently, a series of ordinary differential equations can build established. The polarization curve for ORR can be predicted via solving these equations under different potential[25,52]. Wang et.al predicted a polarization curve for ORR on $Fe(OH)N_4$ and FeN_4 using microkinetic model (**Figure 2.6**). The predicted polarization curve showed a half-wave potential of 0.87 V, close to the measured half-wave potential in experiment.[82]
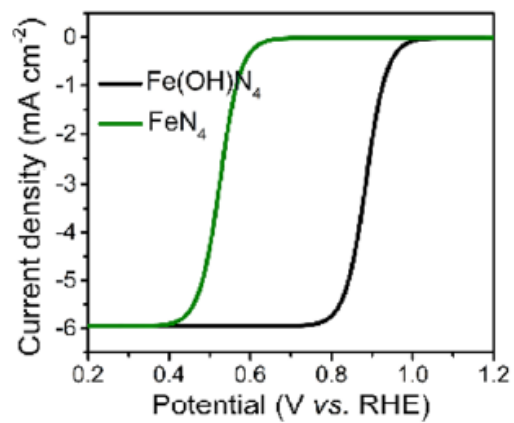
Figure 2.6 Simulated ORR polarization curves on Fe(OH)N$_4$ and FeN$_4$ centers.

3.0 Hypotheses

In this dissertation, the overall hypothesis is:

The MnN$_4$ moieties are the active sites for ORR in Mn-N-C catalyst and the local carbon, nitrogen structure affects the catalytic activity and electrochemical stability of Mn-N-C catalyst.

Moreover, the following detailed hypotheses are examined.

1. The active sites in Mn-N-C catalyst should have a MnN$_4$ moiety. According to the literature review in Section 2.3, FeN$_4$ site has been identified as the active site to promote ORR in Fe-N-C catalyst. Considering that the synthesis procedure of Mn-N-C catalyst is similar to that of Fe-N-C catalyst, it is speculated that the MnN$_4$ moiety is the active site for ORR.

2. **The ORR limiting potential can be determined by the adsorption energy of ORR intermediate *OH.** Based on the discussion in Section 2.2, the relationship between the ORR limiting potential of metal and the adsorption energy of ORR intermediate *OH can be represented as a volcano plot. A similar relation may exist in MnNx sites (x = 2-5).

3. **The adsorption energy of ORR intermediates is correlated with the electronic structure of MnN$_4$ sites**. Based on the d-band theory developed by Norskov et al., the binding strength of an adsorbate on a metal surface depends on the d-band center position relative to the fermi energy.[72] A similar trend may exist in MnNx sites and the modification of local carbon structure could tune the occupation of d orbital.

4. **The stability of MnN$_4$ site should correlate with the bond length between Mn-N bond.** The demetallation was reported as the primary reason leading to the loss of stability in TM-N-C catalyst. The demetallation requires to break TM-N bond, and thus the bond length between Mn-N bond may be a good indicator to evaluate the stability of MnN$_4$ site.

4.0 Objectives

The aim of this dissertation is to test the proposed four hypotheses via systematic computational investigation. Specifically, there are five objectives in this dissertation.

1. Identify the active sites for ORR in Mn-N-C catalyst.

2. Calculate the free energy evolution to investigate the ORR activity on different MnN_x sites. Obtain the relation between the ORR limiting potential of metal and the adsorption energy of ORR intermediate *OH on these sites.

3. Perform electronic structure analysis to gain insight into the reason behind the promising ORR activity of MnN_4 site.

4. Further understand the ORR mechanism on the active sites and explore new method to enhance the activity of active sites. Develop new constant potential method along with microkinetic model to predict the polarization curve of ORR and compare it with experimental result.

5. Calculate the free energy change of demetallation process on MnN_4 active sites. Analyze the correlation between the calculated free energy of demetallation and the Mn-N bond length.

5.0 Computational Method

5.1 Density Functional Theory

Density Function theory (DFT) is a computational quantum mechanical modelling method to investigate the electronic structure of many-body systems[83,84]. DFT bases on two fundamental mathematical theorems. The first theorem proved by Kohn and Hohenberg turns out that the ground-state energy from Schrodinger's equation is a unique functional of the electron density and the derivation of a set of equations by Kohn and Sham. The second theorem points out that the electron density that minimizes the energy of the overall functional is the true electron density corresponding to the full solution of the Schrodinger's equation. The Kohn-Sham equation is shown in **eq.5-1**.

$$\left[-\frac{\hbar^2}{2m}\nabla^2 + V_{ext}(r) + e^2 \int \frac{n(r')}{|r-r'|}d^3r' + V_{XC}(n(r))\right]\Psi_i(r) = \varepsilon_i\Psi_i(r) \qquad \textbf{(5-1)}$$

in which $-\frac{\hbar^2}{2m}\nabla^2$ term represents the kinetic energy, V_{ext} term represents the potential between electrons and nuclei, $e^2 \int \frac{n(r')}{|r-r'|}d^3r'$ represents the Hartree potential describing the potential between electrons, V_{XC} term is the exchange correlation potential, $\Psi_i(r)$ is the wave function of ith electron, and n(r) represents the electron density as a function of position r.

In practical DFT implementations, the exact form of the exchange-correlation potential V_{xc} is unknown, and various approximations are used. The simplest approximation is the Local Density Approximation (LDA), which assumes that the exchange-correlation energy is a function of the local density. More sophisticated approaches are the Generalized Gradient Approximations (GGAs) that include the gradient of the density. There are many forms of GGA functional such as Perdew-Wang 1991 (PW91) and Perdew-Burke-Ernzerhof (PBE). More advanced approximations include the meta-GGA like R2SCAN, hybrid functionals like HSE, and range-separated hybrids that include additional terms. The choice of the exchange-correlation functional can significantly affect the results of DFT calculations, and thus much of the research in DFT involves developing better approximations for V_{xc} term to accurately capture the physics of the electron-electron interactions in a variety of systems. In practice, the choice of functional largely depends on the specific task/system and the budget of the computational resource.

5.2 Computational Hydrogen Electrode Method

As shown in **eq.5-7**, ORR involves multiple proton-coupled electron transfer steps. To predict the free energies of solvated protons and electrons, Nørskov et al. proposed the computational hydrogen electrode (CHE) method, which has been widely used in computational studies of the thermodynamics of electrochemical reactions.[72] Within the CHE method, the free energy of a proton-electron pair is calculated as shown in **eq.5-2**.

$$G(H^+ + e^-) = 0.5G_{H_2} - eU_{SHE} - 2.303 \times k_b T \times pH = 0.5G_{H2} - U_{RHE} \tag{5-2}$$

where G_{H2} represents the calculated free energy of a hydrogen molecule in gas phase under standard condition, U_{SHE} and U_{RHE} represent the applied electrode potential relative to standard hydrogen electrode and reversible hydrogen electrode, respectively, k_b is Boltzmann constant, and T is temperature. Consequently, the CHE method provides a practical approach to correlate charge-neutral DFT calculations in vacuum to the potential-dependent energetics of an electrochemical reaction. So far, the CHE method has been successfully applied to predict the activity for various electrocatalytic reaction.[75,85,86] Especially, Greeley et.al used the CHE method to predict a volcano plot of metal catalysts for ORR.[87] They revealed a relationship between the predicted ORR activity and oxygen adsorption energy, which provides a guidance to the development of metal alloy catalysts for ORR.

5.3 Formation Energy and Adsorption Energy

In this study, the thermal stability of various MnN$_4$ sites is evaluated by calculating their formation energy. It should be mentioned that a lower formation energy represents greater structural stability for the MnN$_4$ site. The formation energy was calculated as:

$$E_f = E_{MnN4} - x\mu_c - 4\mu_N - \mu_{Mn} - y\mu_H \qquad (5\text{-}3)$$

Where, $E_{TM\text{-}N4}$ represents the total energy of TM-N$_4$ site, μ_C represents the chemical potential of carbon atoms defined as the atomic energy of perfect graphene, μ_N represents the chemical potential of nitrogen atoms defined as a half of the total energy of an N$_2$ molecule, μ_{Mn} represents the chemical potential of isolated Mn atom in the gas phase, and μ_H represents the chemical potential of hydrogen atoms defined as a half of the total energy of an H$_2$ molecule.

The adsorption energy of ORR intermediates (denoted as X) on MnN$_4$ site was calculated as:

$$E_{ad} = E_{X-MnN4} - E_{MnN4} - E_X \qquad (5\text{-}4)$$

Where, E_{ad} represents the adsorption energy, $E_{X\text{-}MnN4}$ represents the total energy of the adsorbed system, E_{MnN4} represents the energy of the isolated MnN$_4$ site, and E_X represents the energy of the isolated intermediates X, respectively.

5.4 Computational Setup

In this thesis, the spin-polarized calculations were performed using Vienna Ab-Initio Simulation Package (VASP) code[88,89]. The core electrons were described by Projector augmented wave (PAW) and a cut-off energy of 400 eV was used for plane wave basis[90,91]. The electronic exchange-correlation was described by generalized gradient approximation (GGA) with the Perdew, Burke and Ernzernhof (PBE) functional[92]. The Brillouin Zone was sampled with Monkhorst-pack[93] 4×4×1 k-point mesh for sites MnN_2C_{12}, MnN_3C_9, MnN_3C_{11}, MnN_4C_{10}, FeN_4C_{10}, CoN_4C_{10}, and MnN_5C_{10}, and 3×3×1 k-point mesh for sites MnN_4C_{12}. A vacuum region of over 14 Å was added in the direction normal to the carbon layer to ensure negligible interaction between the slab and its images. In structure optimization calculations, the atomic positions were allowed to relax until the force on each ion fall below 0.02 eV/ Å. The transition states of chemical reaction were located using the climbing image nudged elastic band (CI-NEB) method[94], in which the force along and perpendicular to the reaction path were relaxed to less than 0.05 eV/ Å. Zero-point energy correction, entropy correction and heat capacity corrections were included in all the reported energies using **eq.5-5, 5-6 and 5-7**.

$$ZPE = \sum_i \frac{1}{2} h v_i \qquad \textbf{(5-5)}$$

$$S = k_B * \sum_i \left(\frac{h v_i}{k_B T} * \frac{1}{\exp\left(\frac{h v_i}{k_B T}\right) - 1} - \ln\left[1 - \exp\left(-\frac{h v_i}{k_B T}\right)\right] \right) \qquad \textbf{(5-6)}$$

$$C = k_B * \sum_i \left(\frac{(\frac{h v_i}{k_B T})^2 * \exp\left(-\frac{h v_i}{k_B T}\right)}{[1 - \exp\left(-\frac{h v_i}{k_B T}\right)]^2} \right) \qquad \textbf{(5-7)}$$

Where, T is the temperature of reaction, S is the vibrational entropy, h is the Planck's constant, k_B is the Boltzmann constant, vi is the frequency of the ith vibrational mode, ZPE is the zero- point energy and C is the vibrational heat capacity.

In summary, the free energy change for the chemical reaction was calculated as follows (**eq.5-8**).

$$\Delta G = \Delta E_{DFT} + \Delta E_{ZPE} + \int C(T)dT - T\Delta S \qquad \textbf{(5-8)}$$

where ΔE_{DFT} is the energy change calculated by DFT, ΔE_{ZPE} is the change of zero-point energy, $\int C(T)dT$ is the enthalpy change from 0 to T K, and ΔS is entropy change.

5.5 Constant Potential Method

The computational hydrogen electrode (CHE) method developed by Norskov and co-workers[72], has been applied to successfully explain the ORR activity on various catalytic surfaces. However, the neglect of potential and pH effect in CHE model leads to some predictions that are inconsistent with experimental observations.[95,96] Notably, experimental electrochemical reactions are operated under constant, whereas calculations only using CHE method assume the system at zero net charge. This discrepancy leads to the failure of CHE predictions for some electrochemical reactions. Besides the adsorption of reaction species, the chemical reaction at an electrochemical interface should also include the interaction between adsorbates and the electric field within the electric double layer (EDL). To take these effects into account, the double reference method combined with implicit solvation model is adopted to simulate the EDL under constant potential conditions.[97] This method has proven to be successfully to explain some experimental observations, especially on metal catalyst.[98-100]

The electrode potential of the slab was calculated via relating the work function of the slab to the experimental measured work function of the standard hydrogen electrode (SHE) as shown below.

$$U = \frac{\Phi - \Phi_{SHE}}{e} \tag{5-9}$$

Where Φ and Φ_{SHE} represent the work function of the slab and SHE, respectively. Considering the experimental measured value of Φ_{SHE} (4.2±0.4 eV), the Φ_{SHE} = 4.3 eV was used in this study. The potential-dependent total energy of the charged system is calculated as

$$E_{total} = E_{DFT} + \int_0^q <V_{tot}> dQ - q\Phi \tag{5-10}$$

Where the <Vtot> refers to the average electrostatic potential and Q is excess charge of the unit cell. In **eq.5-10**, the $\int_0^q < V_{tot} > dQ$ term represents the interaction between charged system and compensating background charge, and the $-q\Phi$ term corrects the energy for the difference in the number of electrons in the system. For each structure, DFT calculations were performed at the net charge of -2e to 1e with step of 0.5e. The total energies at the 7 charge states were then used to fit a quadratic function to obtain a continuous function between electrode potential and total system energy. After assuming capacitance of surface consistent, the quadratic function form is shown as

$$E(U) = -\frac{1}{2}C(U - U_0)^2 + E_0 \qquad \textbf{(5-11)}$$

Where U_0 refers to the potential of zero charge (PZC), E_0 is the energy at PZC, and C is the capacitance of the slab.

5.6 Microkinetic Model

The prediction of chemical kinetics on catalysts is important in catalysis research. Following the power-law expression[101], the kinetic rate of a reaction can be calculated as:

$$r_i = k_{f,i} * \prod[reactant]^m - k_{b,i} \prod[product]^n \qquad \text{(5-12)}$$

where r_i is the kinetic rate of the ith elementary reaction, $k_{f,i}$ and $k_{b,i}$ are the forward and backward rate constants for the ith elementary reaction, symbols [reactant] and [product] represent the molar concentration of reactants and products, respectively, m and n are the corresponding exponents for the reactants and products. The forward reaction rate constant can be calculated as:

$$k_{f,i} = A_i \exp\left(-\frac{\Delta G_{a,i}}{k_b T}\right) \qquad \text{(5-13)}$$

whereas the backward reaction rate constant is calculated as:

$$k_{b,i} = A_i \exp\left(-\frac{\Delta G_{a,i} - \Delta G_{f,i}}{k_b T}\right) \qquad \text{(5-14)}$$

where A_i is pre-exponential factor for the ith elementary reaction, k_b is Boltzmann constant, T is temperature, $\Delta G_{a,i}$ is the standard activation energy for the ith elementary reaction, and $\Delta G_{f,i}$ is the free energy change for the ith elementary reaction. The reaction rates of all elementary reactions of ORR are presented in Appendix A.1. These reaction rates could be determined by solving a system of coupled ordinary differential equations (ODEs), which describe the relation between the time variation of the surface concentration θ of reaction intermediates and the reaction rate of each elementary reaction. These ODEs can be solved at steady state where the surface concentration of each chemical species does not change with time and the total number of surface sites are conserved. After the reaction rates of each elementary reaction are obtained, the current density j of an electrochemical reaction is computed as: $j = e\rho TOF_{e^-}$, where e is the charge of

electron, ρ is the surface density of active sites (a typical value of $\sim 6.8 \times 10^{16}$ sites m^{-2} for M-N-C catalysts[102]), and TOF_{e^-} is the turnover frequency of electrons, which is equal to summation of the rates of all the elementary reactions involving electron transfer. Hansen et.al[25] used the microkinetic model to predict a Tafel slope of 59 mV/dec for ORR on Pt(111) surface, in good agreement with experimentally observed Tafel slope (60~88 mV/dec)[103] of Pt catalyst.

6.0 Result and Discussion

6.1 Chemical Nature of Active Sites

Early experimental studies revealed a clear correlation between the content of FeNx moieties and the catalytic activity for ORR of the pyrolyzed Fe-N-C catalysts.[61] However, it is difficult to identify the chemical nature of the active sites for ORR in TM-N-C catalysts. Complementary to experimental effort, the first-principles computational methods were used to predict the ORR activity on various possible TM-Nx moieties embedded in carbon layers. To identify the active site in Mn-N-C catalyst, DFT calculations were performed to examine six different MnNx sites, including fully embedded MnN_2C_{12}, MnN_3C_{11}, MnN_3C_9, MnN_4C_{10}, MnN_5C_{10} sites, and porphyrin-like MnN_4C_{12} site, as shown in **Figure 6.1**. Specifically, the structures of MnN_2C_{12}, MnN_3C_{11}, MnN_4C_{10} and MnN_5C_{10} site were constructed via replacing six carbon atoms with MnN_x site in graphene layer with a unit cell size of 9.84×8.52Å. The MnN_3C_9 site was constructed by substituting four carbon atoms using MnN_3 moiety in graphene layer with a unit cell size of 9.84×8.52Å. The porphyrin like MnN_4C_{12} structure contains a Mn atom binding to four pyrrolic nitrogen atoms with a cell size of 12.42×12.20 Å. For the calculations to investigate the D1 to D2 transformation and the hydrogenation effect, the D1 and D2 MnN₄ moieties were embedded in a larger graphene layer with a cell size of 17.28×12.83 Å. It should be mentioned that these six sites have been studied in Fe-N-C catalyst.[56]
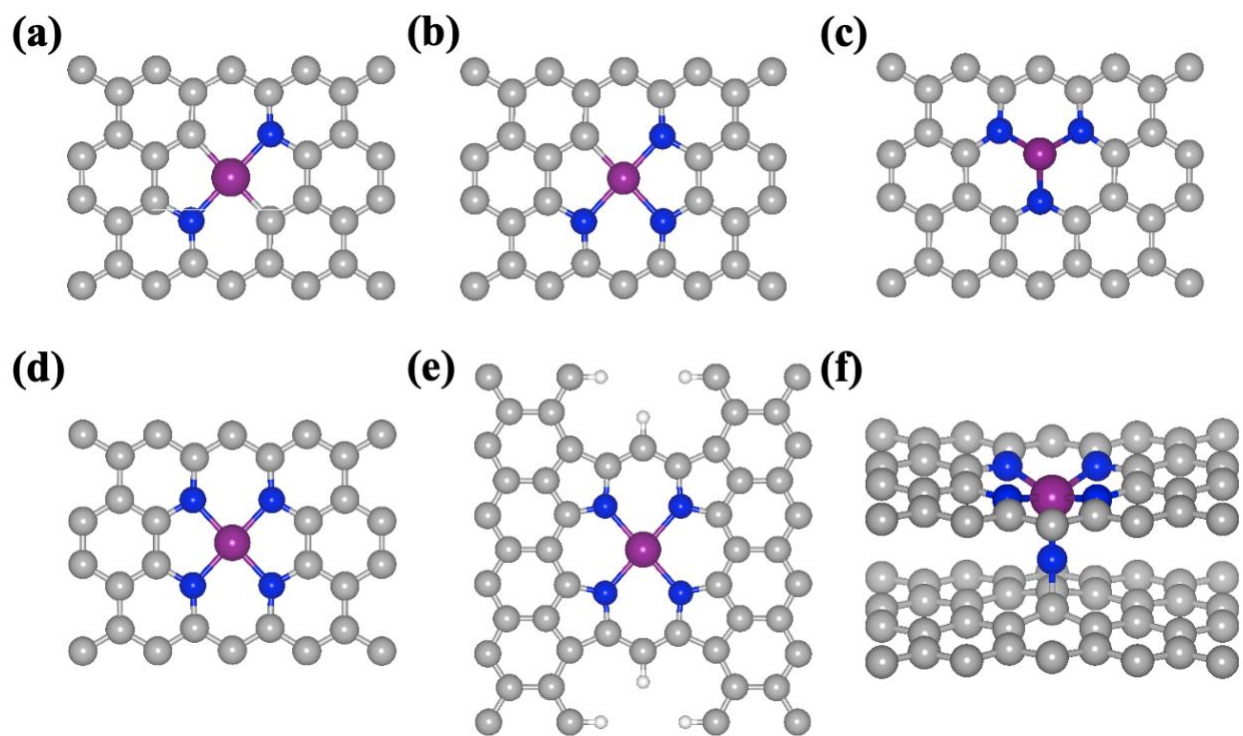
Figure 6.1 Atomistic structures of possible active sites of the Mn-N-C catalysts for ORR. (a) MnN_2C_{12} site, in which a Mn atom bonds with two N atoms and two C atoms, (b) MnN_3C_{11} site, in which a Mn atom bonds with three N atoms and one C atom, (c) MnN_3C_9 site, in which a Mn atom bonds with three N atoms, (d) MnN_4C_{10} site, in which a Mn atom bonds with four N atoms lying on six carbon rings, (e) MnN_4C_{12} site, in which a Mn atom bonds with four N atoms lying on five-carbon rings, and (f) MnN_5C_{10} site, in which a Mn atom bonds with five N atoms (four N atoms in a graphene layer and the fifth N atom lying out of the graphene layer). In this figure, the gray, blue, white, and purple balls represent C, N, H, and Mn atoms, respectively.

6.1.1 Identification via Calculating Adsorption Energy

It is particularly relevant to use the first-principles calculations for prediction of the adsorption energy of chemical species involved in ORR on the MnNx sites with varying chemical structures. The adsorption energy is defined as the energy difference between the adsorbate system and the corresponding isolated systems (See Section 5.3). In order to be an efficient active site for ORR, the MnNx sites must be capable of favorably adsorbing the reactant O_2 to initiate the reaction, as well as readily desorbing the product H_2O to complete it. The optimized adsorption configurations of ORR reactant (O_2), intermediates (OOH, O and OH) and product (H_2O) on the six proposed MnNx sites have been showed in Appendix A.2 and the corresponding adsorption energies are summarized in Table 1. These results indicate that the adsorption energy for O_2 is consistently negative across the MnNx sites, implying favorable adsorption for O_2. However, the adsorption energies for H_2O at the MnN_2C_{12} and MnN_3C_9 sites are strongly negative, exceeding -0.4 eV, which corresponds to the solvation energy of a H2O gas molecule in an aqueous electrolyte.[104] This suggests these sites may have inferior ORR activity. In contrast, our computational findings suggest that MnN_3C_{11}, MnN_4C_{10}, MnN_4C_{12}, and MnN_5C_{10} sites exhibits an appropriate binding strength with the ORR species and thus may serve as the active sites for ORR. These results are in good agreement with the experimental observation of the Mn-N coordination number ranging from 3.2-3.9.[21,105]

Table 1 Predicted adsorption energies of various ORR species on the six MnN_x active sites. Negative value of adsorption energy indicates attractive interaction between the ORR species and active sites.

E_{ad} (eV)	O_2	OOH	O	OH	H_2O
MnN_2C_{12}	- 2.10	- 2.17	- 5.35	- 3.23	- 0.49
MnN_3C_9	- 3.20	- 2.93	- 6.44	- 4.09	- 0.55
MnN_3C_{11}	- 1.75	- 1.59	- 5.05	- 3.06	- 0.36
MnN_4C_{10}	- 1.27	- 1.62	- 4.40	- 2.77	- 0.26
MnN_4C_{12}	- 0.87	- 1.31	- 3.86	- 2.56	- 0.32
MnN_5C_{10}	- 0.26	- 1.08	- 3.37	- 2.28	- 0.02

6.1.2 Identification via Calculating QS Values in Mössbauer Spectroscopy

For Fe-N-C catalysts, [57]Fe Mössbauer spectroscopy serves as a sophisticated technique to investigate the valence state and local structure of Fe. Specifically, the quadrupole splitting (QS) value obtained from Mössbauer spectroscopy is indicative of Fe's local environment and can act as descriptor for this structure. Consequently, the active sites in Fe-N-C catalyst can be identified via comparing the QS value measured in experiment and the QS value predicted on different FeNx sites. As shown in Table 2, the QS values of the FeN_4C_{12} and FeN_4C_{10} sites are predicted to be 0.79 and 2.76, respectively, in line with the QS values of 1.02 and 2.81 in experiment. These findings enable us to identify the FeN_4C_{12} and FeN_4C_{10} sites as the active sites in Fe-N-C catalyst and denoted them as D1 and D2 type FeN_4 site respectively. Furthermore, as mentioned in Section 2, Fe-N-C and Mn-N-C catalysts are expected to have analogous active sites for promoting electrochemical reactions due to similar synthesis processes. Consequently, we identified the MnN_4C_{12} site (D1 type MnN_4 site) and MnN_4C_{10} site (D2 type MnN_4 site) to be the active sites for ORR in Mn-N-C catalyst.

Table 2 Experimental measured and DFT calculated QS value of Fe in the D1 and D2 type of FeN_4 site.

QS value	DFT prediction	Experimental observation
FeN_4C_{12} (D1)	0.79	1.02
FeN_4C_{10} (D2)	2.76	2.81

6.2 Activity Prediction

6.2.1 Intrinsic Activity of MnN₄ Sites

A variety of computational approaches have been developed and applied to predict the activity of the TM-N₄ sites for ORR. The widely employed approach is to calculate the free energy evolution of ORR on the M-N₄ sites using the computational hydrogen electrode method as described in Section 5.2. The free energy evolution for ORR can be obtained by plotting the free energy of all the chemical species involved in ORR following their occurrence order in a given pathway as shown in **Figure 6.2**. The highest electrode potential under which all of the free energy changes along the ORR pathway are exergonic is thus defined as the thermodynamic limiting potential for ORR on the MnN₄ sites. Therefore, a higher limiting potential corresponds to a higher intrinsic ORR activity of the catalyst.
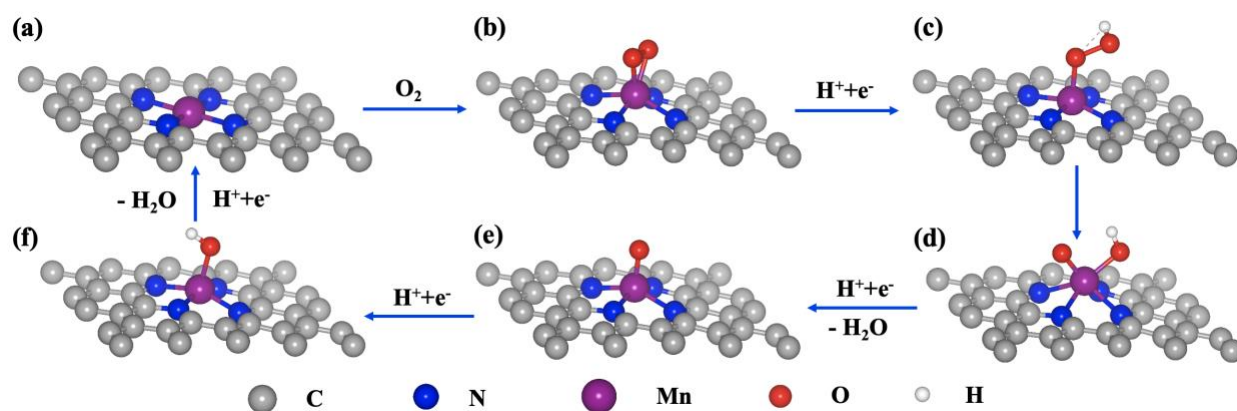
Figure 6.2 Schematics of possible pathways for ORR on a D2 type MnN₄ site embedded in a graphene layer.

As shown in **Figure 6.3**, the D1 and D2 type MnN₄ sites exhibits a great ORR activity with a limiting potential of 0.80 and 0.54 V, respectively. In comparison, other MnNx sites like

MnN$_2$C$_{12}$, MnN$_3$C$_{11}$ and MnN$_3$C$_9$ show a much lower limiting potential, as compared D1 and D2 type MnN$_4$ sites (See Appendix A.3). This result further reveals that two MnN$_4$ sites are the active sites for ORR in Mn-N-C catalyst.
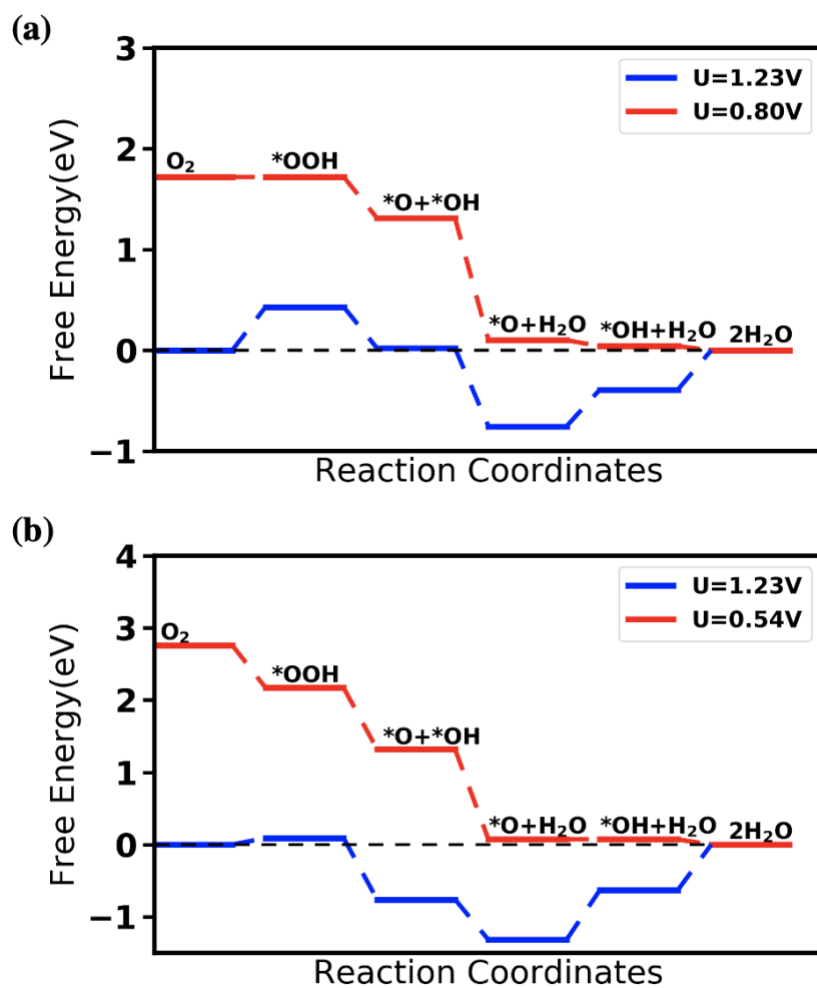
Figure 6.3 Calculated energy evolution diagrams for the ORR on (a) MnN$_4$C$_{12}$ and (b) MnN$_4$C$_{10}$ active sites, respectively, under the electrode potential of U=1.23V and corresponding limiting potential.

6.2.2 Kinetic Activity of MnN$_4$ Sites

Another type of computational approach is to calculate the kinetic activation energy for O-O bond scission process on the M-N$_4$ sites using the nudged elastic band (NEB) method.[94] Given the high dissociation energy of O-O bond in an oxygen molecule (~500 kJ/mol at 298K)[106], the capability to efficiently break O-O bond plays a vital role to promote four-electron ORR. Typically, the O-O bond scission process with an activation energy below 0.90 eV is kinetically feasible on the catalysts surface at 300K.[101] As discussed in Section 2.2, there are three possible non-electrochemical ways to break the O-O bond of O$_2$ molecule adsorbed on a TM-N$_4$ site, namely, O$_2$ dissociation, OOH dissociation and H$_2$O$_2$ dissociation. As shown in **Table 3**, we predicted that the O$_2$ dissociation required an unsurmountable activation energy of 1.82 eV on D1 type MnN$_4$ site and 1.02 eV on D2 type MnN$_4$ site, respectively, implying that direct O$_2$ dissociation might not be feasible on these MnN$_4$ sites. In contrast, the activation energies for OOH dissociation on D1 and D2 type MnN$_4$ sites were predicted to be 0.49 and 0.37 eV, respectively, suggesting the O-O bond scission via OOH dissociation being surmountable at room temperature. As shown in **Figure 6.4**, the central Mn in MnN$_4$C$_{10}$ and MnN$_4$C$_{12}$ site exhibits a capability to break the OOH into O and OH on itself.

Table 3 Calculated activation energies for O$_2$ and OOH dissociation on the D1 and D2 type of MnN$_4$ site.

E_a (eV)	O$_2$ dissociation	OOH dissociation
MnN$_4$C$_{12}$ (D1)	1.82	0.49
MnN$_4$C$_{10}$ (D2)	1.02	0.37

(a)

(b)

| Initial State | Transition State | Final State |
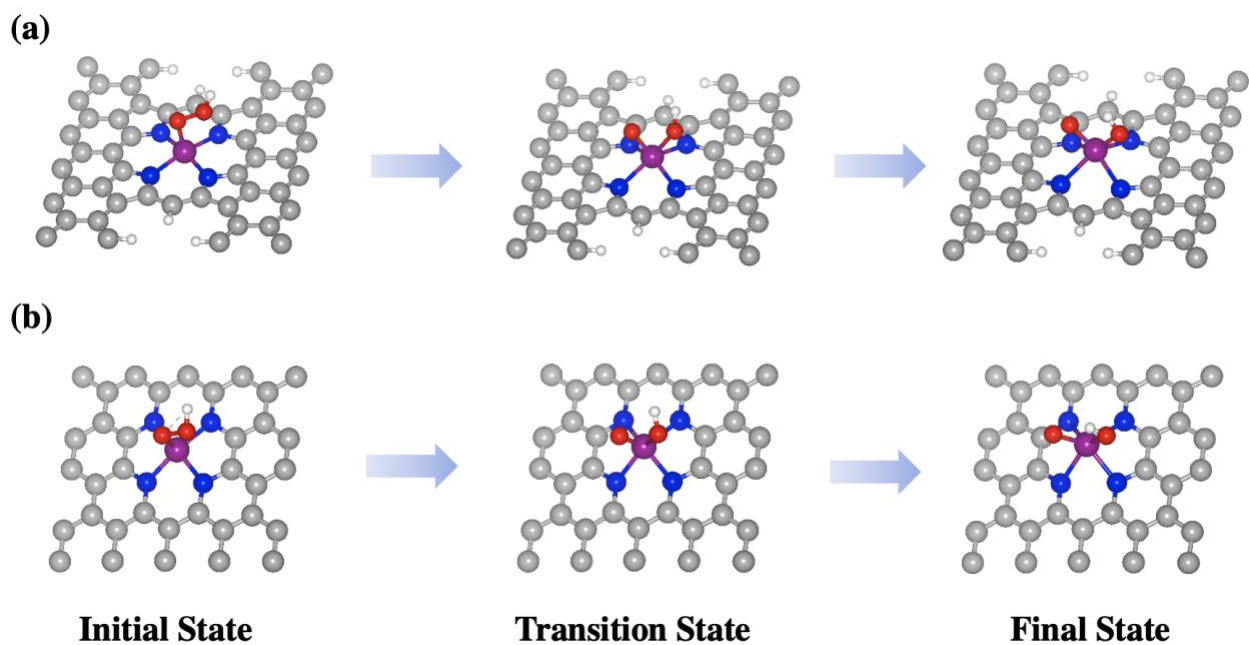
Figure 6.4 Atomistic structures of the initial structure, transition state, and final state for OOH dissociation on (a) D1 type, and (b) D2 type MnN_4 sites. In this figure, the gray, blue, white, red and purple balls represent C, N, H, O and Mn atoms, respectively.

Based on the calculated limiting potentials and activation energies for OOH dissociation, it is concluded that the porphyrin-like D1 type MnN_4 site is more active than D2 type MnN_4 site to promote ORR. It should be noted that D1 type FeN_4 site also exhibits a higher activity than D2 type FeN_4 site, which is turned out by Li et al. using in-situ Mössbauer spectroscopy.[107]

6.2.3 Linear Scaling Relationship and Volcano Plot

Regarding that associative ORR pathway involves three intermediates, it is anticipated that the limiting potential will be influenced by the adsorption energies of these ORR intermediates. Nørskov et al. observed a strong correlation between the adsorption energies of *OOH, *O, and *OH across different metal surfaces, demonstrating a monotonical trend.[72] This linear relationship was attributed to a similar metal–oxygen bond state across these surfaces. Our investigation into MnNx sites revealed a similar linear scaling relationship for the adsorption energies of *OOH, *O, and *OH, as depicted in **Figure 6.5a**. Notably, the slope of the *OOH versus *OH line is approximately 0.9, suggesting a Mn-O single bond being common to both adsorbates. By contrast, the slope for *O versus *OH is close to 2, which implies that *O binds to the MnNx site via a double bond.

Consequently, the predicted limiting potential can be expressed as the function of the adsorption energy of *OH (ΔG_{OH*}), which is named as the volcano plot and depicted in **Figure 6.5b**. Notably, this plot closely resembles that derived from the (111) facet of metal catalysts.[75] Moreover, the predicted points of FeN_4C_{10} site and Pt(111) are near the peak of the volcano plot, implying that the calculated volcano plot aligns well with experimental outcomes. Consequently, we believe that the Mn-N-C catalyst is a desirable ORR catalyst, as evidenced by the position of D1 and D2 type MnN_4 sites near the peak of the volcano plot.

(a)

$$G_{OOH} = 0.90 \times G_{OH} + 0.93$$

$$G_O = 1.65 \times G_{OH} + 0.31$$

(b)

Pt(111)

D2 FeN4

D1 MnN4

D2 MnN4

D2 CoN4

$*OH \rightarrow H_2O$

$O_2 \rightarrow *OOH$
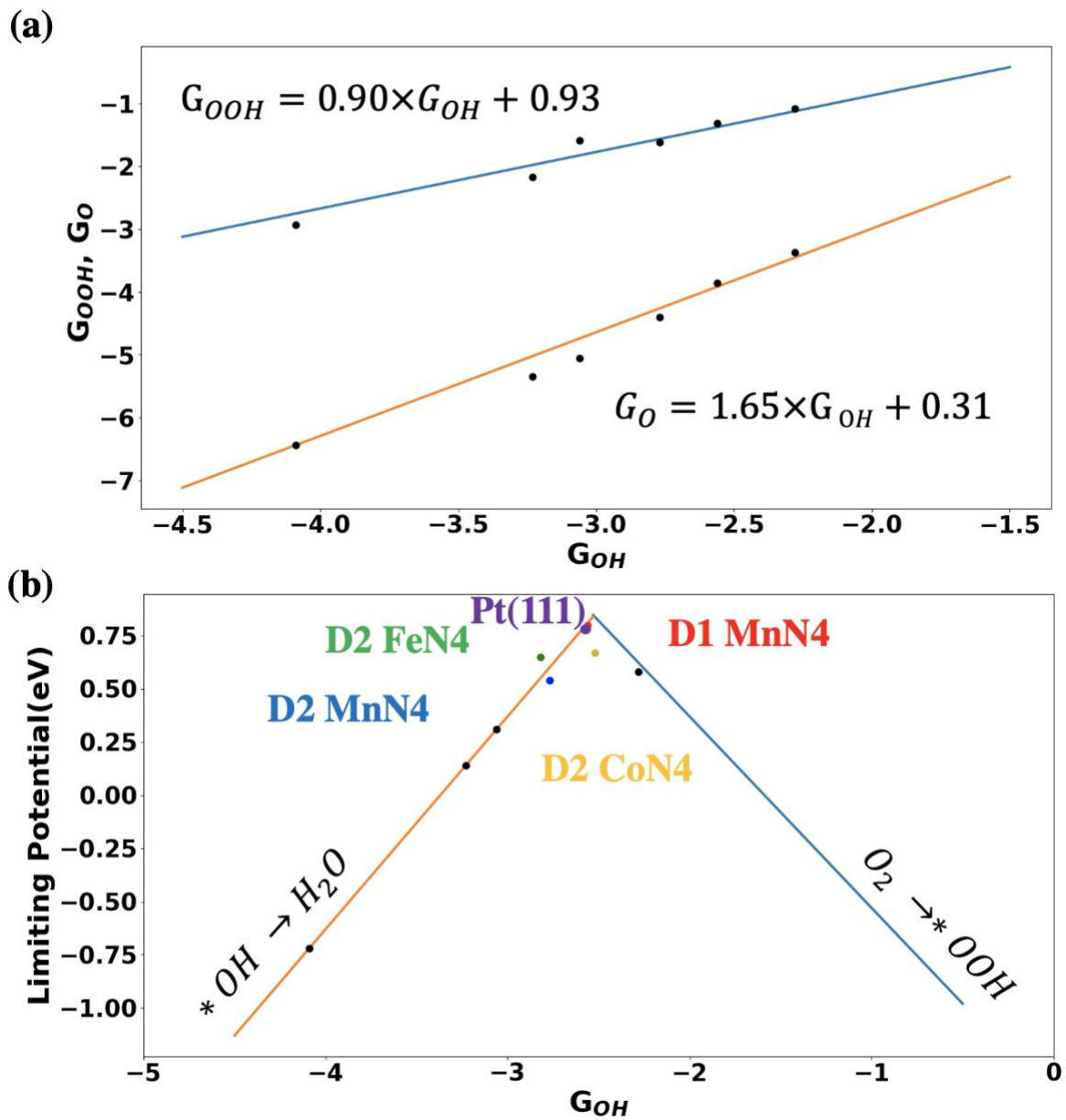
Figure 6.5 (a) Scaling relationships for the adsorption energies of *OOH and *O on MnNx sites using *OH as a descriptor. (b) volcano plot with showing the relation between adsorption energy of OH and limiting potential. The orange line expression is $U_{lim} = G_{OH} + 3.37$, corresponding to the strongly bound OH region. The blue line expression is $U_{lim} = -0.90 \times G_{OH} - 1.43$, corresponding to the weakly bound OOH region.

6.2.4 Electronic Structure of MnN$_4$ Sites

To gain insight into the underlying mechanism of encouraging ORR activity on MnN$_4$ sites, the electronic structure analysis has been performed on D1 and D2 type MnN$_4$ sites. Specifically, we calculated the density of state (DOS) and charge distribution of our modelled D1 and D2 type MnN$_4$ sites.

To elucidate the ORR activity at MnN4 sites, it is crucial to examine the interactions between the Mn atoms within these sites and the O atoms from ORR species. As illustrated in **Figure 6.6**, the bond formation between Mn and O is due to the interactions between the Mn 3d and O 2p orbitals. Importantly, the strength of this interaction is largely determined by the occupancy of the antibonding orbitals, given that the bonding orbitals are fully occupied. Based on the d-band center theory developed by Norskov et al., the binding strength of an adsorbate on a metal surface depends on the d-band center position relative to the fermi energy.[72] Moreover, Liu et al. further turned out that this theory could be extended to the TM-N-C catalyst.[108] Consequently, we calculated the d-band center of D1 type MnN$_4$ site to be -1.18 eV, lower than that of -1.15 eV on D2 type MnN$_4$ site. This result indicates that the central Mn atom in D2 type MnN4 site shows a stronger capability to anchor adsorbates, and thus explains the more negative adsorption energy for ORR intermediates on D2 site than D1 site in **Table 1**.
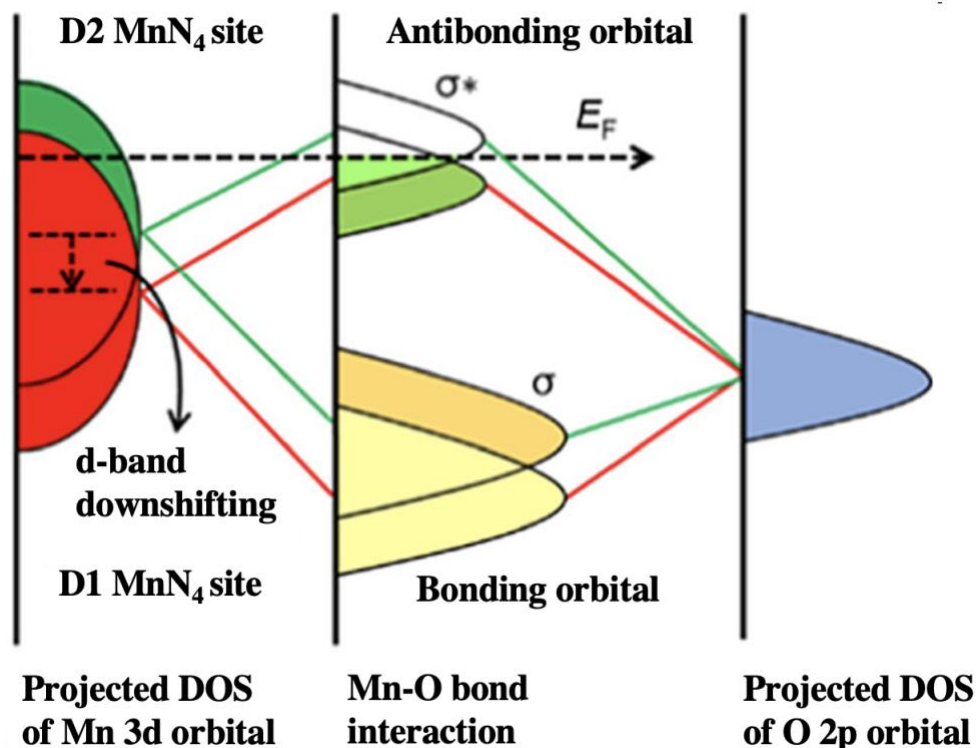
Figure 6.6 Scheme showing bond interaction between Mn 3d orbital and O 2p orbital.

As shown in **Figure 6.7**, the DOS of Mn $3d_{xy}$ orbital is separated into two parts (for example, one part is in the range of -7.5 to -4.5 eV and the other part is in the range of 0 to 1.0 eV for Mn in an D1 type MnN$_4$ site) corresponding to a newly formed bonding orbital and anti-bonding orbital between Mn and its surrounding N, respectively. This result indicates that the central Mn forms chemical bonds with N through Mn $3d_{xy}$ orbital, whereas the other four 3d orbitals (i.e., d_{yz}, d_{xz}, d_{x2-y2}, and d_{z2}) of Mn are non-bonding orbitals which could participate the binding with ORR intermediates. Moreover, we noticed that spin-up anti-bonding orbital of Mn $3d_{xy}$ on an D1 type MnN$_4$ site was very close to fermi energy and could be occupied by electrons (**Figure 6.7a**), whereas all the anti-bonding orbital of Mn $3d_{xy}$ on an D2 type MnN$_4$ site was far away from fermi energy (> 1.5 eV) and would be empty (**Figure 6.7b**). These results reveal that

the Mn-N bond in the D2 type MnN$_4$ site is stronger than that in the D1 type MnN$_4$ site, to some

extent, revealing the higher stability of the D2 type MnN$_4$ site than the D1 MnN$_4$ site.
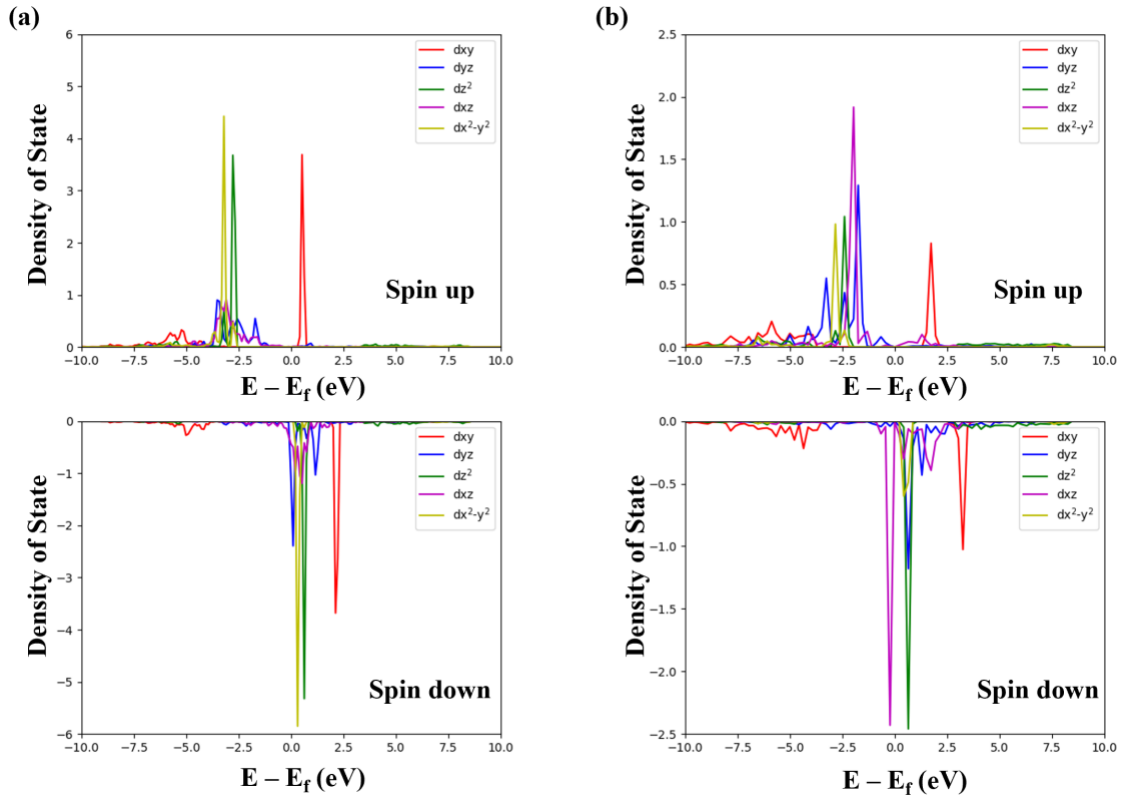
Figure 6.7 Projected density of state of (a) 3d orbitals of the Mn in an D1 type MnN$_4$ site and (b) 3d orbitals of Mn

in an D2 type MnN$_4$ site. In the figure, Ef represents the Fermi energy of the investigated system.
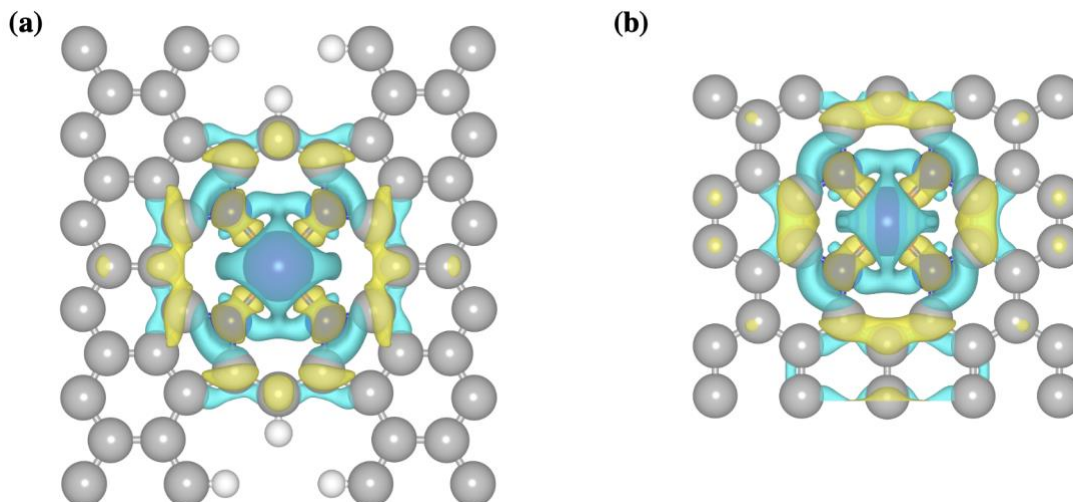
Figure 6.8 Charge density difference for the central part of (a) an D1 type and (b) an D2 type MnN_4 site. The charge density difference is calculated as $\rho(Mn-N_4/C)-\rho(Mn)-\rho(N_4/C)$. Color cyan and yellow represent charge accumulation and depletion in the region, respectively; the iso-surface value is 0.002 e $\mathring{A}^{-3}$.

Figure 6.8 illustrates the charge density distribution, highlighting the influence of Mn-N bonding on the electronic density in the vicinity of MnN_4 sites. Our observations revealed a pronounced charge depletion of Mn on D1 type MnN_4 site, as compared with D2 site. This observation agrees well with the Bader charge analysis result that the net charge of Mn in D1 site (+1.58) is higher than that in D2 site (+1.16). This finding indicates that the central Mn atom in the D2 type MnN_4 site possesses more available electrons for bonding with O_2 and other ORR intermediates compared to the D1 type MnN_4 site. Such a result corroborates our predictions that the D2 type MnN_4 site exhibits stronger adsorption for O_2 and other ORR intermediates.

6.2.5 S Doping for Enhancing ORR Activity of MnN$_4$ Sites

The heterogenous atom doping is a powerful approach to enhance the intrinsic ORR activity in TM-N-C catalyst. In this section, we performed DFT calculations to gain insights into the ORR activity enhancement of the Mn-N-C catalysts by S doping. Based on the discussion in section 6.2.1, the D1 type MnN$_4$C$_{12}$ and D2 type MnN$_4$C$_{10}$ are identified as the most two active sites in Mn-N-C catalyst. We first used D2 type MnN$_4$C$_{10}$ site as example to investigate the doping position of S. To identify the optimal adsorption site of S on MnN$_4$C$_{10}$ site, we compared the system energies of multiple adsorption configurations as depicted in **Figure 6.9** and the corresponding system energies are shown in **Table 4**. We can infer that the single atom S dopant is energetically most favorable to be adsorbed on a bridging site between two carbon atoms adjacent to the D2 type MnN$_4$ site. Consequently, this model (denoted as MnN$_4$C$_{10}$-S) was adopted to model the most possible S doped MnN$_4$C$_{10}$ site. Similarly, we constructed a MnN$_4$C$_{12}$-S site to model the S doped D1 type MnN$_4$C$_{12}$ site as shown **Figure 6.10d**.
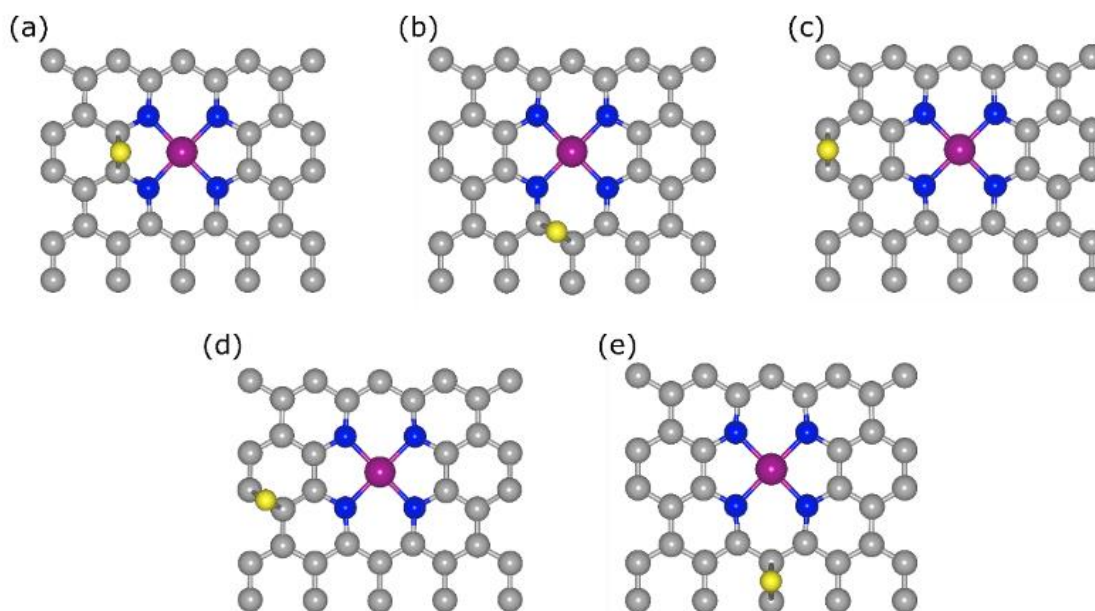
Figure 6.9 Atomic structures of one S dopant adsorbed on a graphene layer containing a MnN_4C_{10} site. In the figure, the gray, blue, purple, and yellow balls represent C, N, Mn, and S atoms, respectively.

Table 4 Calculated system energies of various MnN_4C_{10}-S sites shown in Figure S1 with S adsorbed on different locations. Here, all the given values are the relative energy with respect to that of model (a).

Structures	Relative energy (eV)
(a)	0.00
(b)	0.22
(c)	0.57
(d)	0.69
(e)	1.05

Moreover, we predicted the free energy evolution using four-electron associative ORR pathway on MnN_4C_{10}-S and MnN_4C_{12}-S sites. As depicted in **Figure 6.10**, the limiting potential of the MnN_4C_{10}-S site was predicted to be 0.73 V, 0.19V higher than that on intrinsic MnN_4C_{10} site. This result indicates that doping S could significantly enhance ORR activity on D2 type MnN_4 site. In comparison, the limiting potential of ORR on the MnN_4C_{12}-S and MnN_4C_{12} sites were calculated to be 0.79V and 0.80V respectively, implying that the addition of S dopant would not significantly affect the ORR activity of the D1 type MnN_4C_{12} site.
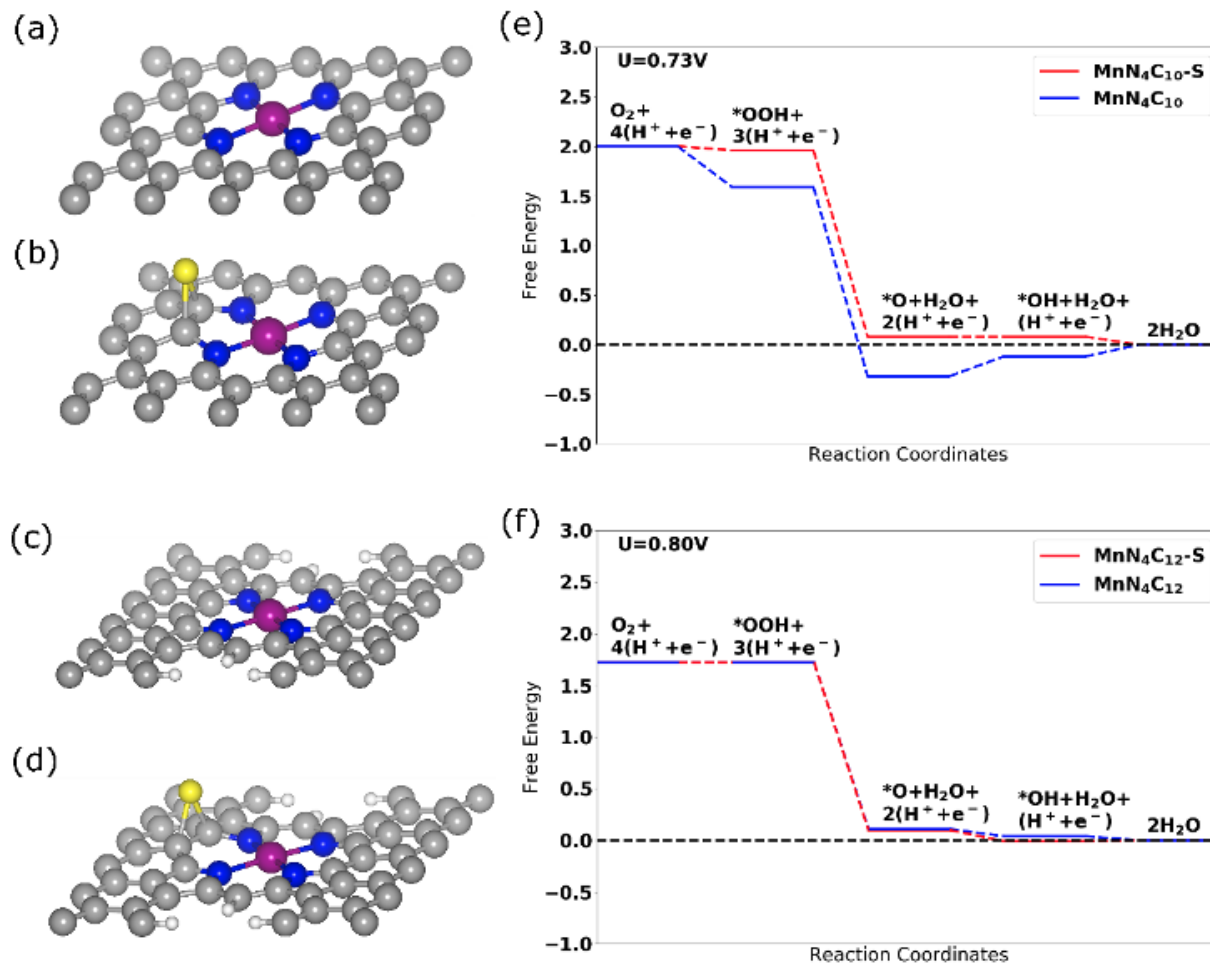
Figure 6.10 Atomic structures of (a) MnN_4C_{10}, (b) MnN_4C_{10}-S sites, (c) MnN_4C_{12}, and (d) MnN_4C_{12}-S. Calculated free energy evolution diagram of ORR following an associative pathway on (e) MnN_4C_{10} and MnN_4C_{10}-S sites at an electrode potential of U=0.73V and (f) MnN_4C_{12} and MnN_4C_{12}-S at an electrode potential of U=0.80V. In the figure, the gray, blue, purple, white and yellow balls represent C, N, Mn, H and S atoms, respectively.

To reveal how the S dopant affecting the ORR activity on the MnN_4C_{10} site, we further conducted the Bader charge analysis to examine the valence charge of the central Mn atom with and without S dopant.[109] The valence charge of the central Mn was precited to be +1.36 on the MnN_4C_{10} site and +1.42 on the MnN_4C_{10}-S site (**Figure 6.11**). This result indicates that S dopant only leads to a small change in the charge state of Mn. Hence, we inferred that the change of

valence charge would not contribute the enhancement of ORR activity significantly. Subsequently, we found a clear spatial repulsion interaction between S dopant and ORR intermediates like *O. This spatial effect derived from the repulsive interaction between S dopant and the ORR intermediate species results in a weakened adsorption of ORR intermediates and hence enhanced ORR activity at the MnN_4C_{10}–S site.
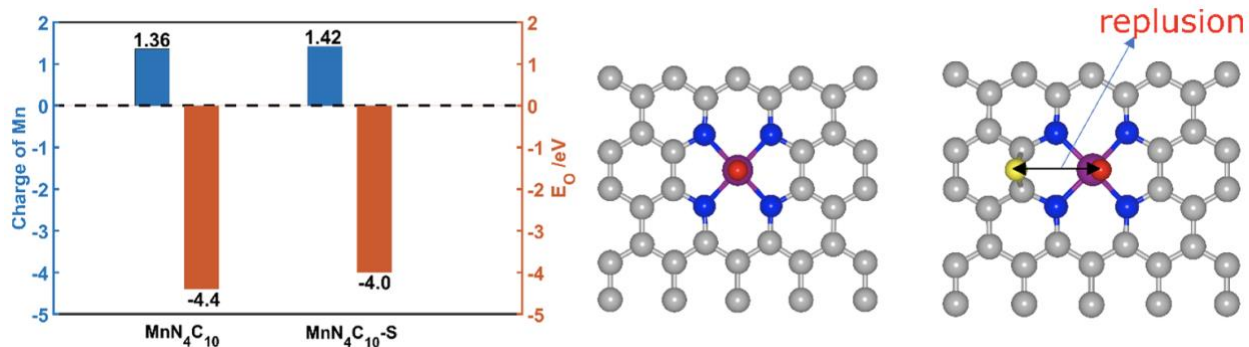
Figure 6.11 Comparison of the calculated valence charge (blue) and adsorption energy of O (orange) on the central Mn atom in MnN_4C_{10} and MnN_4C_{10}-S sites. Optimized atomic adsorption configurations of O on (e) MnN_4C_{10} and (f) MnN_4C_{10}-S sites. In the figure, the gray, blue, purple, and yellow balls represent C, N, Mn, and S atoms, respectively.

6.2.6 Constant Potential Method and Microkinetic Model

As discussed in Section 5.2, the computational hydrogen electrode method has been widely employed to predict the activity of TM-N$_4$ site. However, this method could not provide the relationship between ORR activity and electrode potential or pH value, which is important in experiment. To this end, we developed constant potential method with considering solvation and potential effect to gain insight into the ORR activity on the Mn-N-C and Fe-N-C catalyst.

To understand the relation of adsorption energy and potential, we used the case of OH adsorbed on FeN$_4$ as an example. The atomstic strctures of *OH/FeN$_4$ vary with applied potential as shown in **Figure 6.12**. A most significant structural change is the location of the O atom relative to the Fe atom. The bond length between Fe-O were predicted to be 2.02 Å at U= -0.95 V/SHE, 1.90 Å at U= -0.17 V/SHE, and 1.84 Å at U= 0.94 V/SHE, respectively. This result turns out that Fe-O bond is strengthen with the increase of potential. We found that all of adsorption energies of ORR intermediates on FeN$_4$ site decreases with applied potential increasing. This may ascribe to the increase of potential of zero charge (PZC) and decrease of capacity after oxygenated species adsorbing on TM-N$_4$ site. In addition, we also considered 2e$^-$ ORR pathway in which a O$_2$ molecule would first adsorb on TM-N$_4$ active site then pronoted to form adsorbated OOH and free H$_2$O$_2$ molecule. It should be mentioned that the 2e$^-$ and 4e$^-$ pathways bifracate at the second protonation step. Following 4e$^-$ pathway, the adsorbed OOH would be pronated to form adsorbed O, whereas the H$_2$O$_2$ is generated in 2e$^-$ pathway.
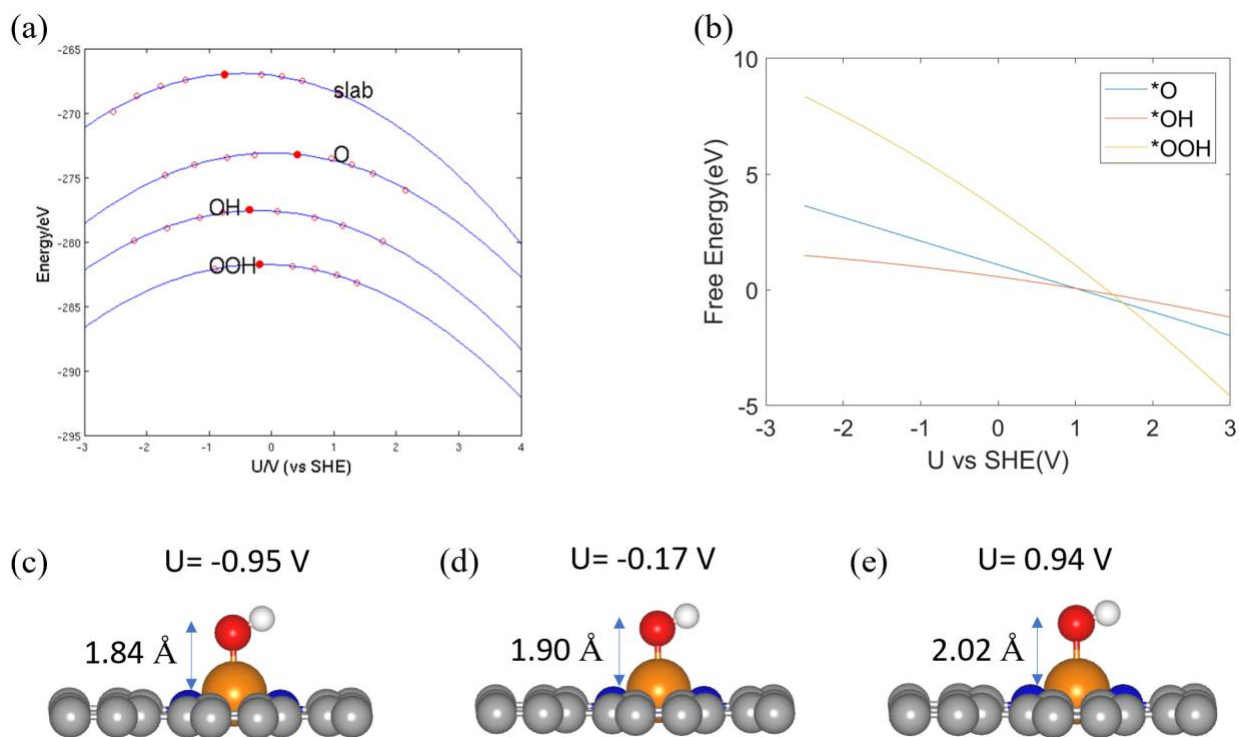
Figure 6.12 (a) Predicted electronic energy of clean site, *OOH, *O, and *OH as a function of applied potential U. The calculated energies are shown in circles, and polynomial fits to these energies are shown using solid line. (b) Predicted adsorption energy of OOH, OH and O as a function of potential. Atomic structures of *OH/FeN$_4$ site under the electrode potential of (c) -0.95 V, (d) -0.17 V, and (e) 0.94 V. In the figure, the gray, blue, orange, red, and white balls represent C, N, Fe, O, and H atoms, respectively.

Based on the calculated adsorption energy, we predicted the free energy evolution following four-electron associative ORR pathway on FeN$_4$ and MnN$_4$ site as shown in **Figure 6.13**. The limiting potential defined as the highest potential at which the free energy evolution become downhill, were predicted to be 0.91V and 0.73 V on D2 type FeN$_4$ and MnN$_4$ site. This result suggests that FeN$_4$ site shows a higher ORR activity than MnN$_4$ site, in good agreement with experimental observation of higher current density at 0.8 V for Fe-N-C catalyst.[50] As compared to previous theoretical predictions for the ORR limiting potential of 0.65 V for FeN$_4$ and 0.54 V for

MnN$_4$ site, our predictions are closer to expermental measured onset potential of 1.00 V for FeN$_4$ and 0.95 V for MnN$_4$.
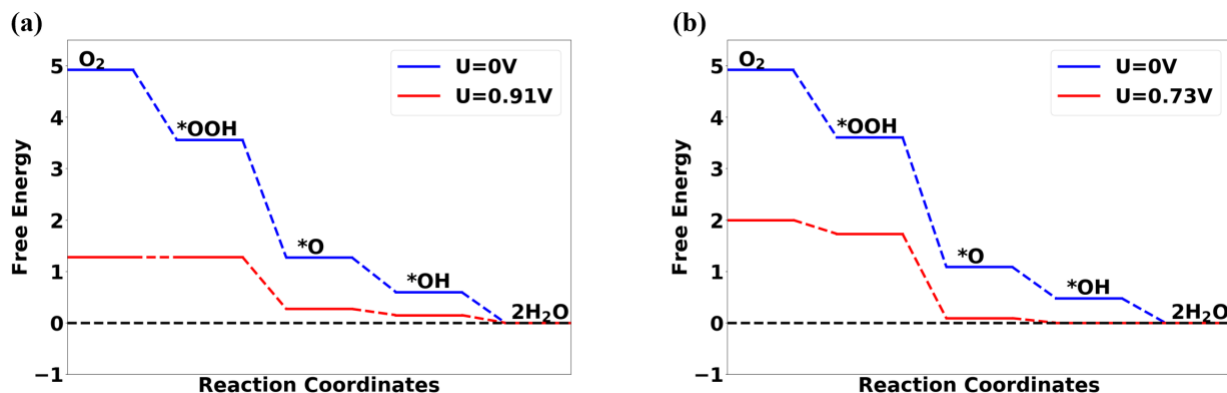
Figure 6.13 Calculated free energy evolution diagrams for ORR through associative pathway on (a) FeN$_4$ and (b) MnN$_4$ active site under electrode potential of 0 V and corresponding liming potential in acid medium (pH=0).

Section 6.2.3 highlights the importance of O-O bond cleavage through OOH dissociation as a critical step in ORR. In this study, we utilized the NEB calculations to identify the transition state and estimate the activation energy for the OOH dissociation reaction. As illustrated in **Figure 6.14**, our findings show that the activation energy for the OOH dissociation reaction increases with the applied potential. Specifically, on MnN$_4$ sites, the activation energy is predicted to be below 0.5 eV within a potential range of 0 to 1.0 V, suggesting that the OOH dissociation step is kinetically viable at room temperature. In contrast, the energy barrier for OOH dissociation is expected to rise above 0.75 eV at applied potentials exceeding 0.8 V, indicating that the O-O bond cleavage at FeN$_4$ sites becomes challenging at higher potential ranges (greater than 0.8 V).[110] This finding provides a good explaination for a relatively high peroxide selectivity at high electrode potential for Fe-N-C catalyst.[110]
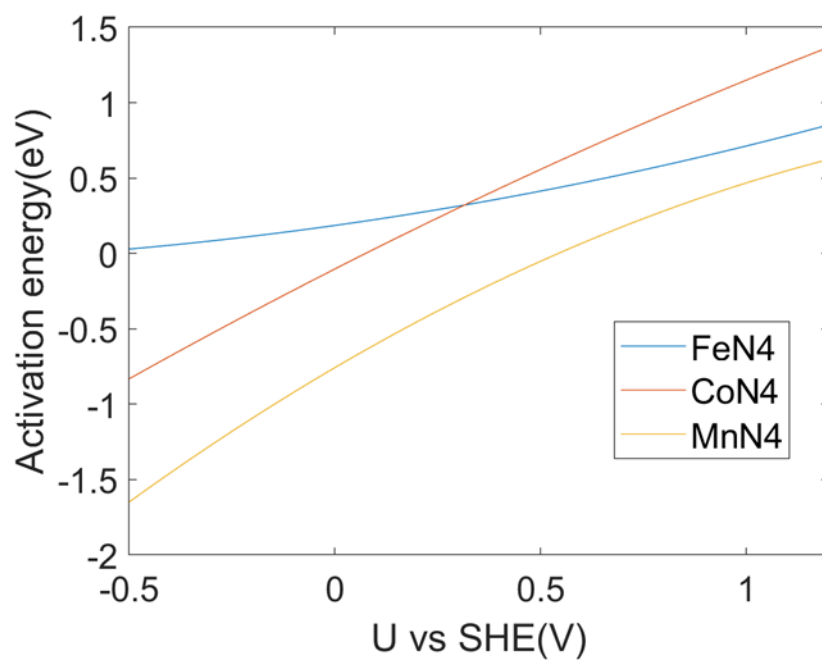
Figure 6.14 DFT predicted activation energy for OOH dissociation reaction on FeN$_4$ and MnN$_4$ sites.
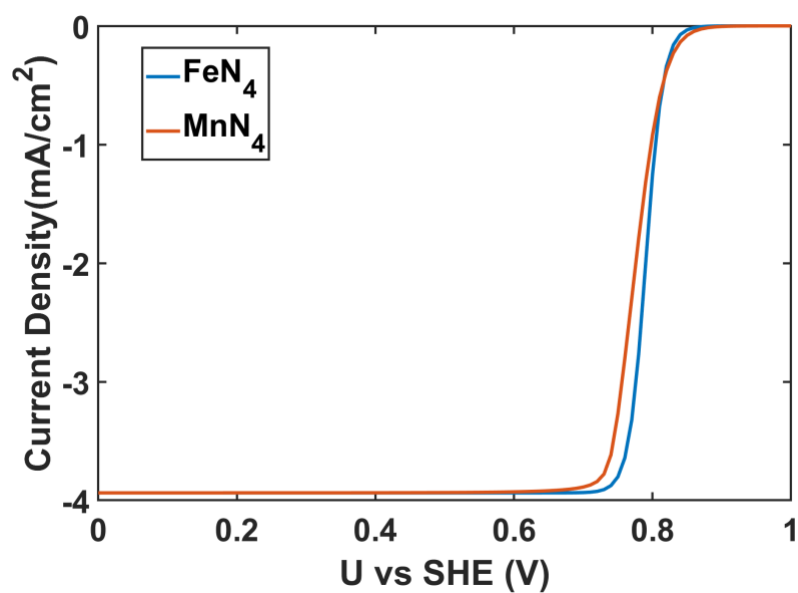
Figure 6.15 Polarization curves for ORR on FeN$_4$ and MnN$_4$ predicted from our microkinetic model.

In order to directly compare our computational predictions with experimental results, we adopted a microkinetic model to predict kinetic rate of ORR on the FeN_4 and MnN_4 active sites. As shown in **Figure 6.15**, the half-wave potentials were predicted to be 0.79 V on FeN_4 site, and 0.73 V on the MnN_4 site, respectively. These predictions differ from experimental value of 0.10 V on FeN_4 and 0.09 V on MnN_4 site, as shown in **Table 5**. It should be noted that previous approach predicts a much lower half-wave potential of ~0.60 for FeN_4 site[111], implying that our model could provide a more accurate prediction for the observed ORR activity in experiment. Meanwhile, our prediction for the number of transferred electrons is 4.00 for both FeN_4 and MnN_4, consistent with experimental measurement of high n>3.9 for Fe-N-C and Mn-N-C catalyst.

Table 5 Measured half-wave potential, DFT predicted half-wave potential and DFT predicted number of transferred electrons for ORR on FeN_4 and MnN_4 sites.

	Half-wave potential_DFT (V)	Half-wave potential_exp (V)	Number of transferred electrons
FeN_4	0.79	0.89	4.00
MnN_4	0.73	0.82	4.00

6.3 Stability Prediction

Understanding how activity is declining during ORR, i.e., the stability of the electrocatalyst under even static *in situ* conditions, is a topic of growing importance in the platinum group metal (PGM)-free ORR electrocatalyst community.[22,112] Computational modeling of M-N-C electrocatalyst active site stability during ORR has taken a variety of approaches. Early efforts focused on relative thermodynamic stability of varied active site structures with reference to lone-metal or bulk-metal reference states.[113] While the formation energy values that resulted are valuable for qualitatively comparing the relative stability of possible sites, the ubiquitous pyrolysis steps used in synthesis that imbue higher ORR activities suggests that realized active sites are in fact metastable. More recent approaches for understanding stability focused on specific degradation mechanisms. As depicted in **Figure 6.16**, the proposed activity loss mechanisms include[114]: dissolution of the central metal atom in the active sites under acidic environments such as PEMFC cathodes; local N- and C-degradation which may alter the local electronic structure and binding energetics and therefore impact calculated activity pathways or promote further degradation; local poisoning of the active site center itself or of the local C environment, serving to sterically block the active site; and finally, ionomer degradation/repartitioning that strands given active sites, starving them of access to reactant protons. Among these mechanisms, the dissolution of the central metal atom, which is also known as demetallation, was reported as the primary reaction for activity loss during ORR. In this section, we performed DFT calculations to investigate the demetallation process on TM-N$_4$ site.
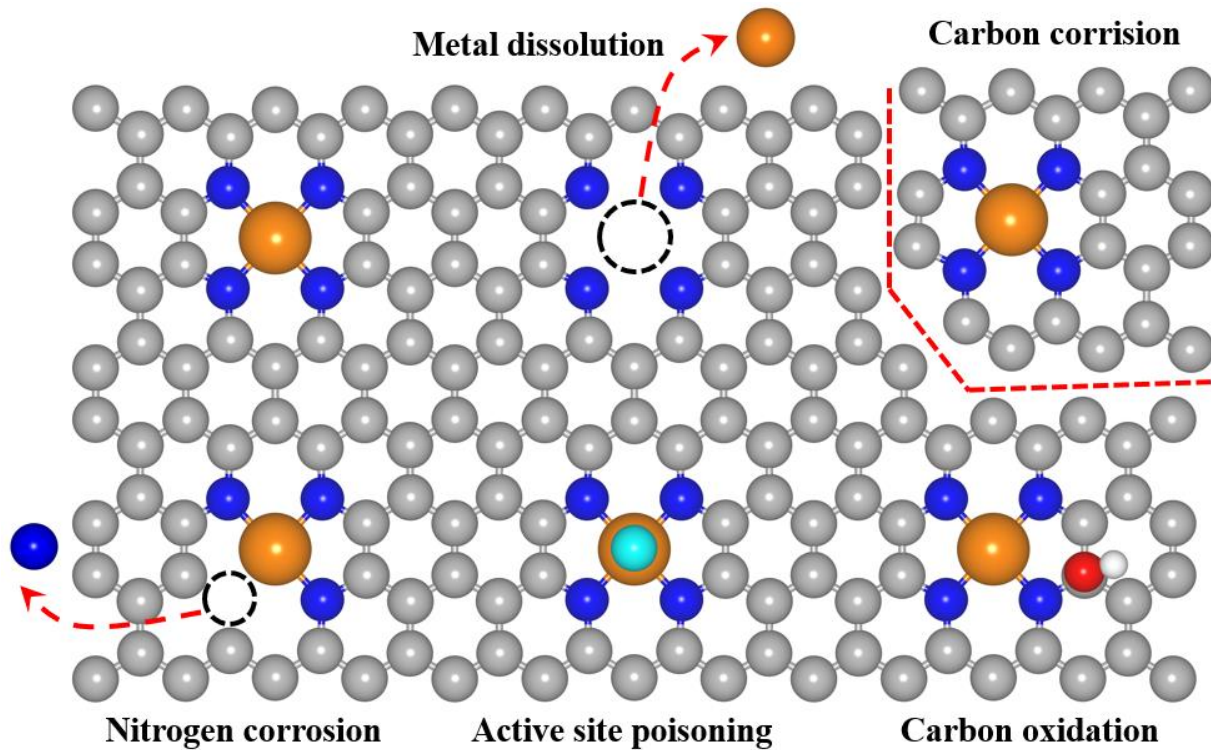
Figure 6.16 Schematics of various degradation mechanisms on TM-N$_4$ site. In this figure, the grey, blue, orange, red, cyan and white balls represent C, N, TM, poison, O, and H atoms, respectively.

6.3.1 Intrinsic Stability for MnN$_4$ Sites

In this section, DFT calculations were carried out to explore the demetallation process on TM-N$_4$ site (including Mn-N-C, Fe-N-C, and Co-N-C).
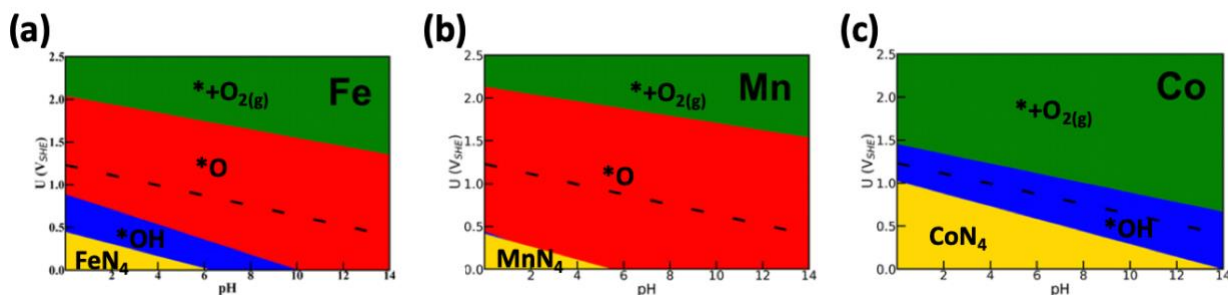
Figure 6.17 Pourbaix diagram for MN$_4$ (M=Mn, Fe, or Co) active sites. It shows the most stable state of adsorbates in given pH and U.

Based on the result of pourbaix diagram for D2 type TM-N$_4$ site (**Figure 6.17**)[115], we found that the clean surface was predicted to be the most stable species at pH=0 and low potential (< 0.5 V). In contrast, the FeN$_4$ would be covered by OH and MnN$_4$ would be covered by O at high potential (0.5 – 1.0 eV). To reflect the stability of TM-N-C under different electrode potential, we compared the stability against demetallation on the clean, oxygen-species terminated, and oxygen-molecule adsorbed MnN$_4$, CoN$_4$ and FeN$_4$ sites. **Figure 6.18** and **Figure 6.19** shows the demetallation process of Mn atom from D1 and D2 type MnN$_4$ sites, respectively. Here, we assumed that the tendency of demetallation from a metal-N$_4$ site could be gauged by the free energy change for a process that the central atom is replaced by two protons and hence lose its four coordination of N. The free energy change for these processes can be calculated by comparing the energies before and after the demetallation and considering the free energy of proton as ½ H$_2$ gas

in acid media based on CHE. It is noted that a positive value of the free energy change indicates a barrier whereas a negative value indicates a driving force for the process.

Tables 6 and 7 present the calculated free energy changes for the demetallation process as depicted in **Figures 6.18** and **6.19**, respectively. For the pristine D1 type sites, the demetallation processes for MnN_4, CoN_4, and FeN_4 are predicted to require surmounting a substantial free energy barrier of 2.72 eV, 3.43 eV, and 3.10 eV, respectively. These high energy barriers indicate that demetallation is unlikely to occur on clean $TM-N_4$ sites, corroborating the findings from long-term stability tests. Notably, the predicted free energy changes for demetallation from oxygen-species terminated and oxygen-molecule adsorbed $TM-N_4$ sites are considerably lower, suggesting that these processes are more likely to contribute to the activity degradation in TM-N-C catalysts.

Our calculated free energy change for demetallation results indicate that the oxygen-species terminated MnN_4 is 0.50 eV more stable than the oxygen-species covered FeN_4 site, and oxygen-molecule adsorbed MnN_4 is about 0.07 eV more stable than the oxygen-molecule adsorbed FeN_4 site. The oxygen-molecule adsorbed CoN_4 shows a highest stability among three $TM-N_4$ sites, with a free energy change of 0.58 eV. Extended this computational approach to D2 type $TM-N_4$ sites, we obtained a consistent trend of catalyst stability, with CoN_4 exhibiting the greatest resilience, followed by MnN_4 and FeN_4. Thus, it can be concluded that CoN_4 and MnN_4 sites possess better stability against demetallation compared to the FeN_4 site, which is in good agreement with experimental data. Furthermore, our findings indicate that the D1 site is less stable than the D2 site when the $TM-N_4$ site is covered by an oxygen molecule, aligning with in-situ observations of D1 site degradation.[65]
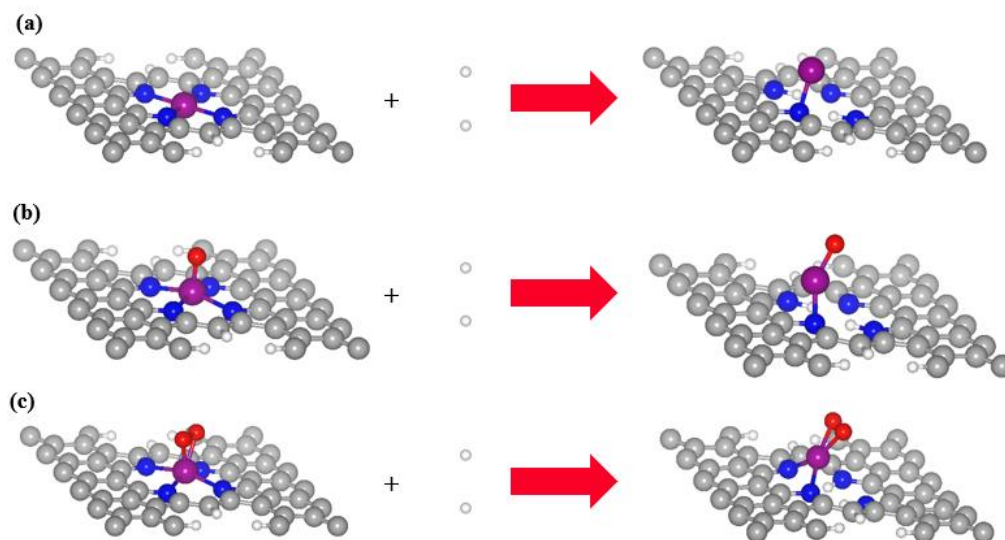
Figure 6.18 Atomistic models showing the demetallation process of Mn atom from (a) a D1 type MnN_4 site, (b) an oxygen terminated D1 type MnN_4 site, and (c) an oxygen molecule adsorbed D1 type MnN_4 site. In the figure, the gray, blue, purple, red, and white balls represent C, N, Mn, O, and H atoms, respectively.

Table 6 Free energy changes for the demetallation process on D1 type MnN_4, CoN_4 and FeN_4 active site.

Free energy change (eV)	clean	Oxygen species-terminated	Oxygen molecule-adsorbed
MnN_4	2.72	1.34	0.50
CoN_4	3.43	-	0.58
FeN_4	3.10	0.84	0.43
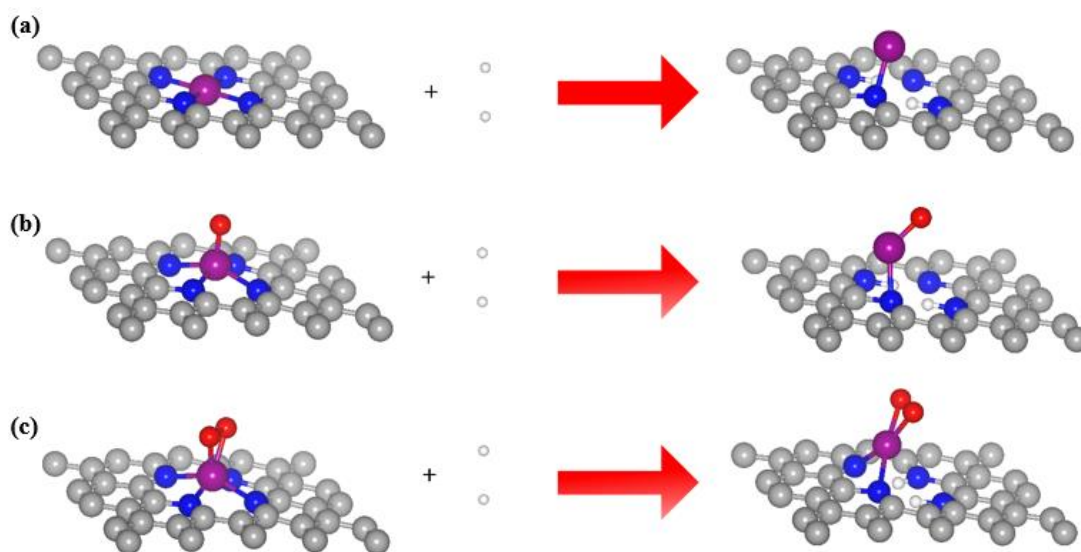
Figure 6.19 Atomistic models showing the demetallation process of Mn atom from (a) a D2 type MnN_4 site, (b) an oxygen terminated D2 type MnN_4 site, and (c) an oxygen molecule adsorbed D2 type MnN_4 site. In the figure, the gray, blue, purple, red, and white balls represent C, N, Mn, O, and H atoms, respectively.

Table 7 Free energy changes for the demetallation process on D2 type MnN_4, CoN_4 and FeN_4 active site.

Free energy change (eV)	clean	Oxygen species-terminated	Oxygen molecule-adsorbed
MnN_4	2.98	1.84	0.86
CoN_4	2.70	-	1.04
FeN_4	3.38	1.33	0.76

6.3.2 Strain Effect on the Stability of TM-N$_4$ Sites

In consideration of the demetallation process that involves breaking the TM-N bond, we examined the relationship between the TM-N bond length and the free energy change of the demetallation process. In this study, we induced small strains on our model to manipulate the TM-N bond length, as depicted in **Figure 6.20**. We observed that a reduction in the Mn-N bond length from 2.01 to 1.94 Å resulted in an increase in the free energy change for demetallation from an O$_2$ adsorbed MnN$_4$ site, rising from 0.50 to 0.80 eV. Likewise, a decrease in the TM-N bond length led to a free energy change increase of 0.22 eV for the FeN$_4$ site and 0.32 eV for the CoN$_4$ site. These findings suggest that a shorter TM-N bond correlates with a higher stability of the TM-N$_4$ site against demetallation.
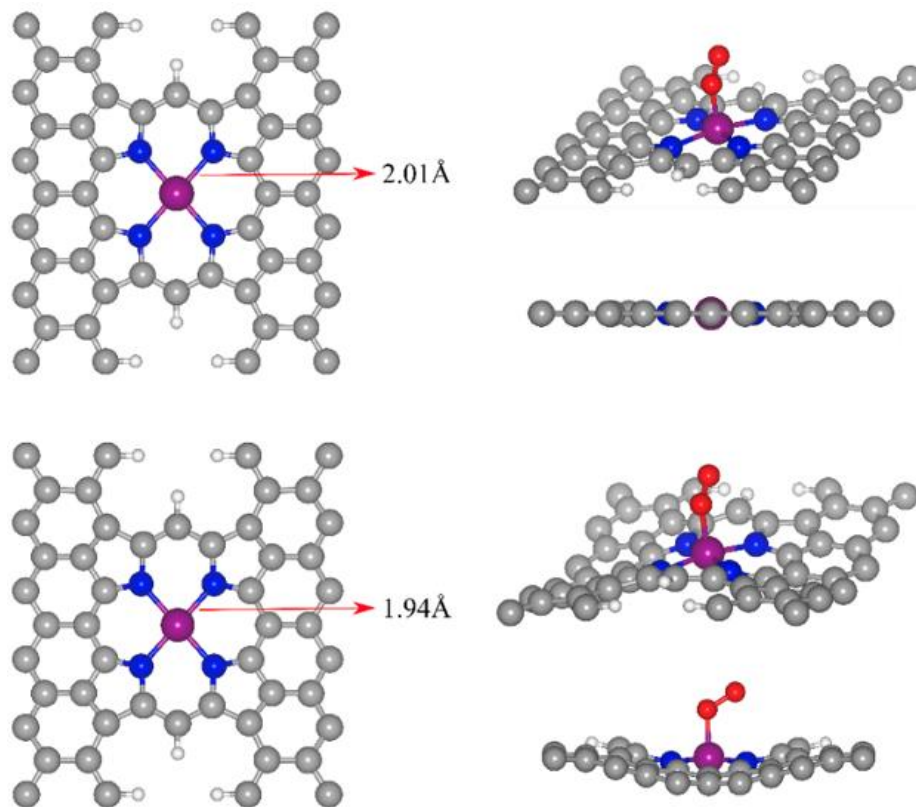
Figure 6.20 Atomistic structures of simulation models of D1 type TM-N$_4$ site with an TM-N bond length of 2.01Å (top) and 1.94Å (bottom), and their corresponding O$_2$ adsorption configurations on the TM sites. In the figure, the gray, blue, purple, red, and white balls represent C, N, M (Mn, Fe, and Co), O, and H atoms, respectively.

6.3.3 Hydrogenation to Enhance the Stability of MnN$_4$ Sites

The findings from Section 6.3.2 indicate that the TM-N bond length serves as a reliable measure for assessing the stability of TM-N$_4$ sites. It was noted that applying a global compressive strain could improve the resistance of TM-N$_4$ sites to demetallation. However, manipulating this global strain is challenging for TM-N-C catalysts, which typically exist in a powder or ink form. Therefore, inducing a local strain in the vicinity of the TM-N$_4$ sites to alter the TM-N bond length emerges as a more practical approach (**Figure 21**). In this work, we explored the effect of hydrogenation on the stability of the MnN$_4$ site.
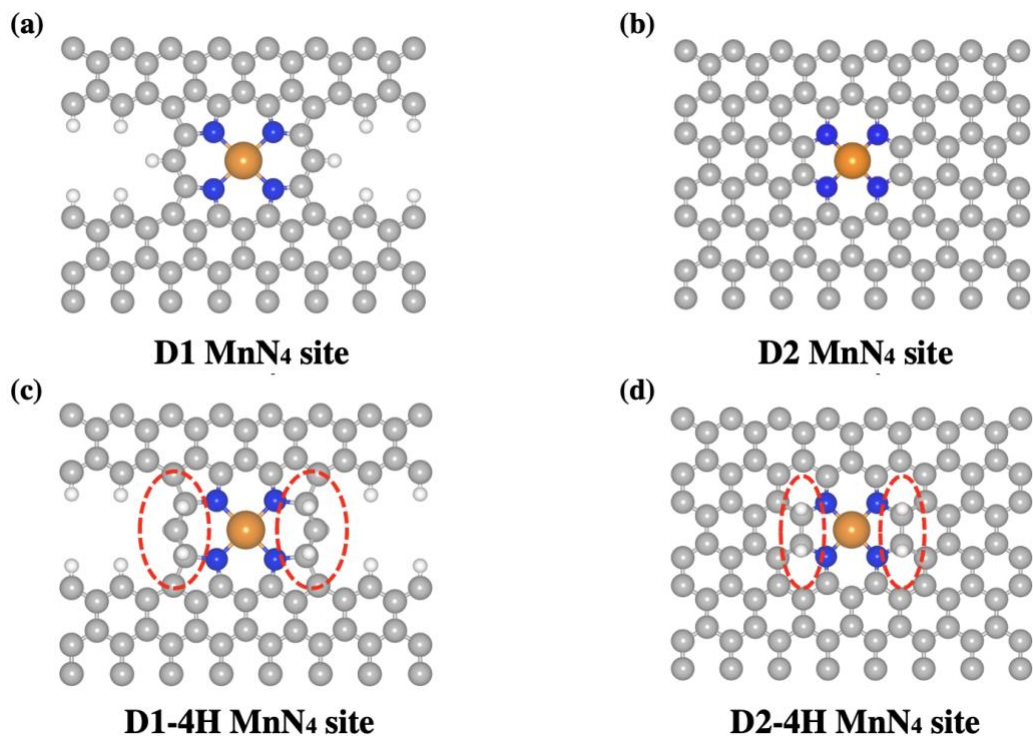
Figure 6.21 Atomistic structures of (a) D1 MnN$_4$ site, (b) D2 MnN$_4$ site, (c) D1-4H MnN$_4$ site, and (d) D2-4H MnN$_4$ sites. In the figure, the gray, blue, orange, red, and white balls represent C, N, Mn, O, and H atoms, respectively.

Our findings revealed that the Fe-N bond length is 2.10 Å in the D1-type MnN$_4$ site and shortens to 2.06 Å in the hydrogenated D1-4H site. Similarly, for the D2 MnN$_4$ site, the Mn-N bond length decreases marginally from 1.92 Å to 1.91 Å upon the introduction of 4H. The Gibbs free energy for the demetallation process is calculated to be 0.02 eV for the D1 type MnN$_4$ site, which is lower than the 0.30 eV for the D1-4H site, as listed in **Table 8**. These results suggest that the stability of the D1 site against demetallation can be significantly improved by hydrogenating the adjacent carbon atoms around the MnN$_4$ moiety, which is also associated with the Mn-N bond contraction due to H$_2$ adsorption. In contrast, the D2-4H site shows a Gibbs free energy for the demetallation process of 1.09 eV, only slightly higher than that of 1.01 eV of the D2 type MnN$_4$ site, unveiling that the incorporation of hydrogen would enhance the stability of D2 site against demetallation just to a small degree. This computational insight can be attributed to a more substantial reduction of the Mn-N bond length by 0.04 Å in the D1 site compared to a reduction of about 0.01 Å in the D2 site following hydrogen attachment to the carbon.

Table 8 Mn-N bond length and calculated free energy for the demetallation process on D1, D1-4H, D2, D2-4H MnN$_4$ sites, respectively.

Site	Mn-N bond length (Å)	Free energy for the demetallation process (eV)
D1 MnN$_4$	2.10	0.02
D1-4H MnN$_4$	2.06	0.30
D2 MnN$_4$	1.92	1.01
D2-4H MnN$_4$	1.91	1.09

6.4 Investigation of Transformation Path from D1 to D2 Site in Mn-N-C Catalyst

D1 and D2 type MnN_4 sites have been identified as the active sites to promote ORR in Mn-N-C catalyst. Experimental evidence has shown that these two types of sites coexist in Mn-N-C catalysts, with their ratio being influenced by the synthesis method. In this section, we first proposed a potential transformation pathway from D1 to D2 site and assessed the thermal stability of these sites by calculating their respective formation energies. Furthermore, we computed the energy barrier for the transition from pyrrolic to pyridinic nitrogen within the MnN_4 framework to better understand the kinetic dynamics of the D1 to D2 site transformation.
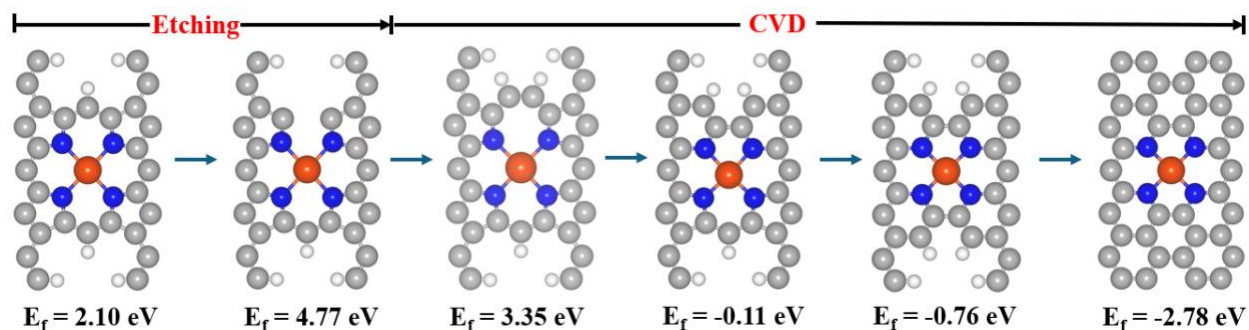
Figure 6.22 Possible structural evolution pathway from an D1 to an D2 site. The grey, blue, white and orange balls represent C, N, H and Mn atoms, respectively. E_f denotes free energy. Blue arrows represent possible structural evolution pathway.

DFT calculations were first conducted to shed light on the possible D1 to D2 transformation pathway from the thermodynamic point of view (**Figure 6.22**). At first, the calculated formation energy of the D2 site is more negative than the D1 site, suggesting that this

conversion is thermodynamically favorable. The defect-rich D1 site could undergo a series of structural change during the pyrolysis process at high temperature such that a transformation of pyrrolic nitrogen into pyridinic nitrogen could occur by deposition of carbon atoms into vacant sites.
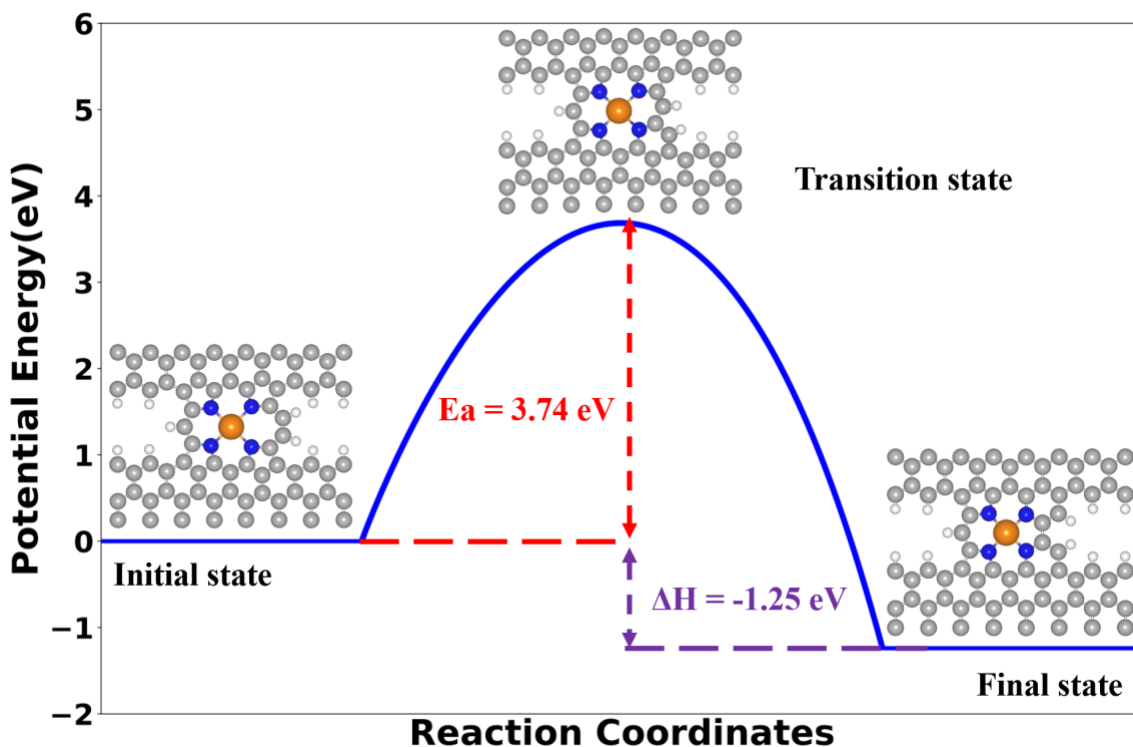
Figure 6.23 Energy evolution for the transition process from a pyrrolic nitrogen to a pyridinic nitrogen in MnN_4 site. In the figure, the gray, blue, orange, and white balls represent C, N, Mn, and H atoms, respectively. E_a and $\triangle H$ represent the activation energy and enthalpy change for the transition process, respectively. The dash circle highlights the area involved in the transition process from a pyrrolic nitrogen to a pyridinic nitrogen.

In this transformation path, the transition from pyrrolic nitrogen to pyridinic nitrogen is a pivotal step. Consequently, the kinetic process of the transition from pyrrolic nitrogen to pyridinic nitrogen has been investigated and its energy barrier has been predicted to be 3.74 eV using NEB method (**Figure 6.23**). This barrier requires a high temperature over 1000 °C to overcome,

explaining why a higher pyrolysis temperature could enhance the graphitization of Mn-N-C catalyst.

7.0 Conclusions and Prospects

7.1 Conclusions

In summary, the chemical nature of active sites, catalytic activity for ORR, and electrochemical stability of Mn-N-C catalyst have been investigated using DFT computational methods. Inspired by the TEM and XAS results, multiple MnNx sites including MnN_2C_{12}, MnN_3C_{11}, MnN_3C_9, MnN_4C_{10}, MnN_4C_{12}, and MnN_5C_{10} have been studied. By analyzing the adsorption energy and formation energy of MnN_x site, the D1 type MnN_4C_{10} and D2 type MnN_4C_{12} site were identified as the active sites for ORR in Mn-N-C catalyst.

Moreover, DFT calculations were carried out to predict ORR activity on these sites. The calculated free energy evolution for ORR indicates that D1 type MnN_4 site exhibits a promising limiting potential of 0.80 V, higher than that of 0.54 V on D2 type MnN_4 site. This result reveals that D1 type MnN_4 site is more active than D2 site to promote ORR. The NEB calculations were performed to indicate that O-O bond session should occur at OOH step and the corresponding activation energy for OOH dissociation were predicted to be 0.49 eV on D1 and 0.37 eV on D2 site, respectively, unveiling $4e^-$ ORR being kinetically feasible on both sites. The volcano plot further pointed out the ORR activity could be estimated by calculating the adsorption energy of ORR intermediates and two MnN_4 sites showed encouraging ORR activity as alternatives to replace Pt catalyst. Moreover, the electronic structure analysis was performed to gain insight into the encouraging activity of MnN_4 sites. In particular, the enhanced ORR activity on D1 type MnN_4 site as compared with D2 site, was ascribed to its relatively low d-band center. To enhance the

activity of Mn-N-C catalyst, sulfur doping effect was predicted to be beneficial to improve the intrinsic activity of D2 type MnN_4 site.

In addition, a constant potential method combined with a microkinetic model was developed and applied to predict the ORR activity on the MnN_4 sites. The relation between adsorption energy of ORR intermediates and applied potential was illustrated as a quadratic function. The activation energy for OOH dissociation was predicted to increase with the applied potential rising. Microkinetic model was adopted to generate the polarization curve of ORR on D2 type MnN_4 and FeN_4 sites. The half-wave potentials were predicted to be 0.73 V on MnN_4 site and 0.91 V on FeN_4 site, respectively, closely aligning with the experimental measured values and significantly improved as compared with results from traditional DFT calculations.

Furthermore, the first principles DFT calculations were carried out to investigate the electrochemical stability of Mn-N-C catalyst. The free energy change for demetallation process was used to assess the stability of MnN_4 site. The DFT calculations revealed that the introduction of O_2 on MnN_4 site could largely decrease the free energy change for demetallation process, implying an inferior stability of MnN_4 site under oxygen atmosphere. The free energy changes for demetallation process were predicted to be 0.50 eV for D1 type MnN_4 site and 0.86 eV for D2 type MnN_4 site, implying D2 site being more stable than D1 site against demetallation. This finding was ascribed to the stronger Mn-N bond in D2 site, as compared with that in D1 site, according to the electronic structure analysis. The introduction of compressive strain was found to enhance the stability of MnN_4 site via strengthening the Mn-N bond. The incorporation of hydrogen could introduce a small local compressive strain near MnN_4 site and thus enhance the intrinsic stability of MnN_4 site.

Finally, we investigated the transformation path from D1 to D2 site to examine novel synthesis concept for enhancing the electrochemical stability of Mn-N-C catalysts. It was found that D2 site was thermodynamically more stable than D1 site via comparing their formation energies. The transition from pyrrolic nitrogen to pyridinic nitrogen, which is considered as the key step in D1 to D2 transformation, requires to overcome an energy barrier of 3.74 eV, implying this transition would occur at temperature over 1000 °C.

In conclusion, this study presents a promising approach for developing active and stable catalysts for ORR by leveraging a synergy between computational analysis and experimental investigation. Initially, experimental characterizations facilitate the computational efforts to screen and identify the active sites for ORR. Subsequently, computational studies can probe the ORR mechanism on these identified active sites, enabling predictions about their activity and stability. Furthermore, supplemental analyses, such as the examination of electronic structures, can provide deeper insights into the factors driving ORR performance and thus guide experimentalists to synthesize effective ORR catalyst. Specifically, the interplay between computation and experiment can be highlighted in four specific aspects: (1) MnN_4 sites were computationally identified as the active sites for ORR, guiding experimentalists to utilize metal-organic frameworks containing $Mn-N_4$ moieties as precursor to synthesize Mn-N-C catalyst. This approach has led to encouraging ORR performance of Mn-N-C catalyst. (2) Computational analysis has shed light on why some Mn-N-C catalysts show high activity but less stability, whereas others exhibit better stability but reduced activity. (3) Computational stability investigations have improved our understanding of the Mn-N-C catalyst performance under oxygen atmosphere, revealing reasons for its inherent instability under such conditions. (4) The predicted free energy evolution has provided a possible strategy for experimentalists to synthesize catalysts with a high D2/D1 ratio,

aiming for optimized catalytic performance. These insights can then inspire innovative strategies for the experimental design of ORR catalysts with superior performance. This integrative strategy—integrating experimental and computational methodologies, alongside iterative measurement and validation—empowers researchers to profoundly understand the ORR mechanism and synthesize catalysts with excelling functionality.

7.2 Prospects

Despite considerable advancements in the development of TM-N-C catalysts, there remain challenges to further enhance the activity and stability of ORR in both experimental and computational studies. This section will explore these challenges along with corresponding prospects, from both experimental and computational perspectives.

Many recent experimental results demonstrated that TM-N-C catalysts achieved a high turnover frequencies comparable to those of commercial platinum-based catalysts.[46] . Computational studies have similarly revealed that the intrinsic ORR activity of the D1 type MnN_4 site rivals that of Pt(111). Nevertheless, a significant challenge remains: the active site density of platinum-based catalysts is approximately an order of magnitude higher than that of TM-N-C catalysts. Consequently, a critical hurdle in advancing TM-N-C catalysts is to increase the density of $TM-N_4$ active sites to approach those in platinum-based counterparts. Currently, transition metal concentrations in TM-N-C catalysts have been reported to be below 1 at %.[20,21] Attempts to increase the loading of transition metals using conventional synthesis methods often result in the undesirable agglomeration of metals, leading to a decrease in $TM-N_4$ active site availability. Therefore, it is essential to explore innovative synthesis techniques that can enhance transition metal loading without causing severe agglomeration. Addressing this issue is pivotal in harnessing the full potential of TM-N-C catalysts for practical applications. In computational study, it is essential to examine those thermodynamic factors which may limit the total density of active sites. For example, evaluating the binding energy of the N_4 moiety to the transition metal against the binding energy of transition metals in nanoparticles can offer insights into the thermodynamic driving force of agglomeration.

Another obstacle related to developing TM-N-C catalyst in experiment is to control the transformation of TM-N_4 active site. Given that D1 and D2 type MnN_4 sites exhibit distinct ORR activities and stabilities, as well as requiring different enhancement strategies, developing a synthesis method that yields a TM-N-C catalyst with a high proportion of either D1 or D2 sites is critical. For example, Wu et al. have shown the possibility to regulate the ratio of D1/D2 FeN_4 sites by modulating the pyrolysis atmosphere.[50] They discovered that the Ar/H_2 pyrolysis atmosphere could tip the balance in favor of the D2 site, with D1/D2 ratio shifting from 1.56 to 0.92 upon the integration of hydrogen. Nevertheless, this modification falls short of achieving a Fe-N-C catalyst composed solely of the D2 site, indicating that significant work remains to refine the D1/D2 ratio further. In computational study, the binding energies between N_4 moieties and transition metal in D1 and D2 sites can be compared, using the difference as a benchmark. The potential effect of doping with other heteroatoms such as sulfur (S), phosphorus (P), and boron (B) can be computationally explored, and the corresponding binding difference will be compared with the benchmark. This comparison may reveal their influence on the transition between D1 and D2 sites, and thus pave way for tuning D1/D2 ratio.

As for computational methodology, many mainly focus on thermodynamics, whereas it is kinetics that ultimately determines the reaction rate. Accuracy in calculating reaction kinetics for specific structures is crucial for unraveling the details of catalytic site structure and reaction mechanisms. Therefore, it is important to develop first-principles kinetic models that balance high accuracy with manageable computational demands. For example, Liu et al. developed a constant potential-hybrid solvation-dynamic model method which samples both atomic structures and charge states along reaction pathways, thus providing kinetic information.[81] However, this method requires a substantial number of computationally intensive ab-initio molecular dynamics

calculations and thus limits its application to smaller systems with limited sampling density. A promising solution lies in substituting the quantum mechanical characterization of atomic interactions with force fields—a more economical alternative that allows for extensive calculations in larger systems with dense sampling. Currently, the application of machine learning (ML) force fields derived from DFT databases has shown promising results. [116,117] Nevertheless, these ML potentials are typically specialized for particular systems. Therefore, the construction and generalization of a robust ML potential is essential. Such a potential would significantly enhance our capability to simulate the electrochemical interface.

Appendix A Appendices and Supplemental Content

Appendix A.1 Elementary Step, Kinetic Rate, and Ordinary Differential Equation in Microkinetic Model

The elementary steps as well as the corresponding reaction rates in the microkinetic model are listed in this section. In these equations, * represents the active site, x represents mole fraction, θ represents surface concentration, r is the net rate of reaction, k_f and k_b represent forward and backward reaction rate constant, respectively.

At beginning, the dissolved O_2 molecules would diffuse from the electrolyte to the catalyst-electrolyte interface, which is also named as electric double layer (DL).

$$O_{2(aq)} \rightarrow O_{2(dl)}, \quad r_1 = k_{f,1}x_{O2(aq)} - k_{b,1}x_{O2(dl)}$$
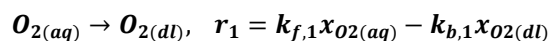
Subsequently, the O_2 molecule in DL would be adsorbed on the vacant active site.

$$O_{2(dl)} + * \rightarrow * O_2, \quad r_2 = k_{f,2}x_{O2(dl)}\theta_* - k_{b,2}\theta_{O2}$$
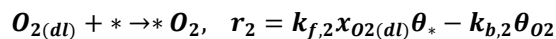
Once the O_2 molecule is adsorbed on the active site, the ORR would proceed following the associative four-electron ORR pathway. These equations are listed below.

$$* O_2 + H^+ + e^- \rightarrow * OOH, \quad r_3 = k_{f,3}\theta_{O2} - k_{b,3}\theta_{OOH}$$

$$* O + H^+ + e^- \rightarrow * OH, \quad r_4 = k_{f,4}\theta_O - k_{b,4}\theta_{OOH}$$

$$* OH + H^+ + e^- \rightarrow H_2O_{(aq)} + *, \quad r_5 = k_{f,5}\theta_{OH} - k_{b,5}\theta_*$$

$$* OOH \rightarrow * O - OH, \quad r_6 = k_{f,6}\theta_{OOH} - k_{b,6}\theta_{O-OH}$$

$$* O - OH + H^+ + e^- \rightarrow * O + H_2O_{(aq)}, \quad r_7 = k_{f,7}\theta_{O-OH} - k_{b,7}\theta_O$$

$$* OOH + H^+ + e^- \rightarrow * H_2O_2, \quad r_8 = k_{f,8}\theta_{OOH} - k_{b,8}\theta_{H2O2}$$

$$* H_2O_2 \rightarrow H_2O_2 + *, \quad r_9 = k_{f,9}\theta_{H2O2} - k_{b,9}x_{H2O2}\theta_*$$
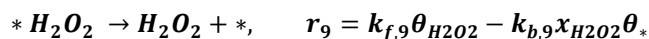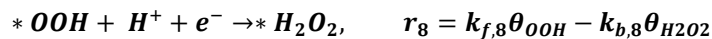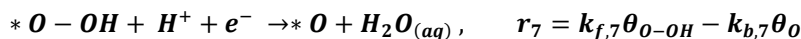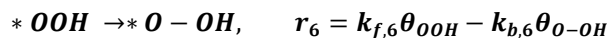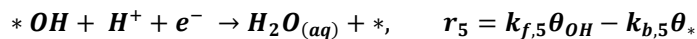
These reaction rates are coupled with each other via rate equations describing the time variation of the surface species concentration:

$$\frac{\partial x_{O2(dl)}}{\partial t} = r_1 - r_2$$

$$\frac{\partial \theta_{O2}}{\partial t} = r_2 - r_3$$

$$\frac{\partial \theta_{OOH}}{\partial t} = r_3 - r_6 - r_8$$

$$\frac{\partial \theta_O}{\partial t} = r_7 - r_4$$

$$\frac{\partial \theta_{OH}}{\partial t} = r_4 - r_5$$

$$\frac{\partial \theta_{O-OH}}{\partial t} = r_6 - r_7$$

$$\frac{\partial \theta_{H2O2}}{\partial t} = r_8 - r_9$$

Meanwhile, the site conservation on the catalyst surface should be satisfied.

$$\theta_* + \theta_{O2} + \theta_{OOH} + \theta_{O-OH} + \theta_O + \theta_{OH} + \theta_{H2O2} = 1$$

The aforementioned equations can be solved numerically at steady state where the concentration of each intermediate is invariant with respect to time. The parameters involved in this work can be obtained in previous reference.[25]
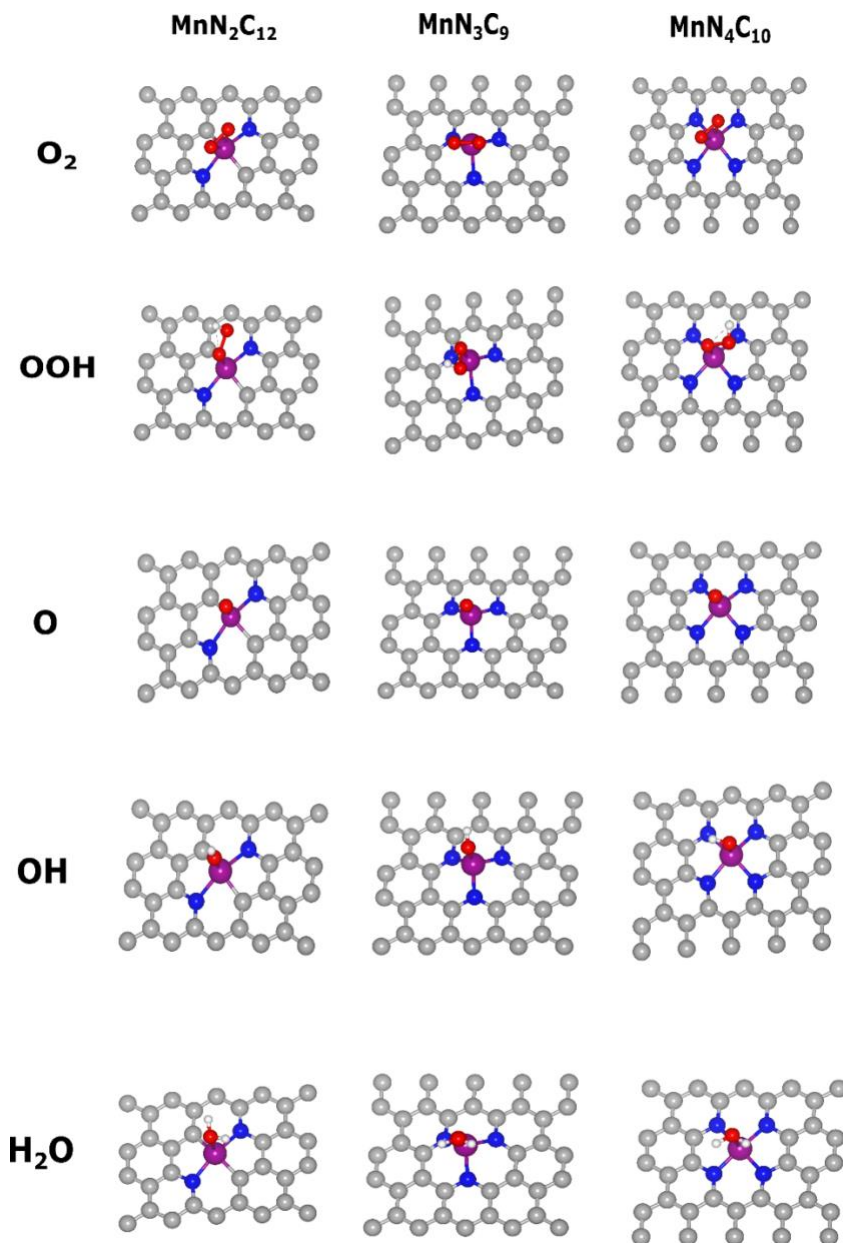
Figure 7.1 Atomistic structures of the optimized configurations of various ORR species adsorbed on the three MnN$_x$-types active sites. Column 1-3: MnN$_2$C$_{12}$, MnN$_3$C$_9$, and MnN$_4$C$_{10}$; Row 1-5: O$_2$, OOH, O, OH, and H$_2$O. In this figure, the gray, blue, purple, red, and white balls represent C, N, Mn, O, and H atoms, respectively.
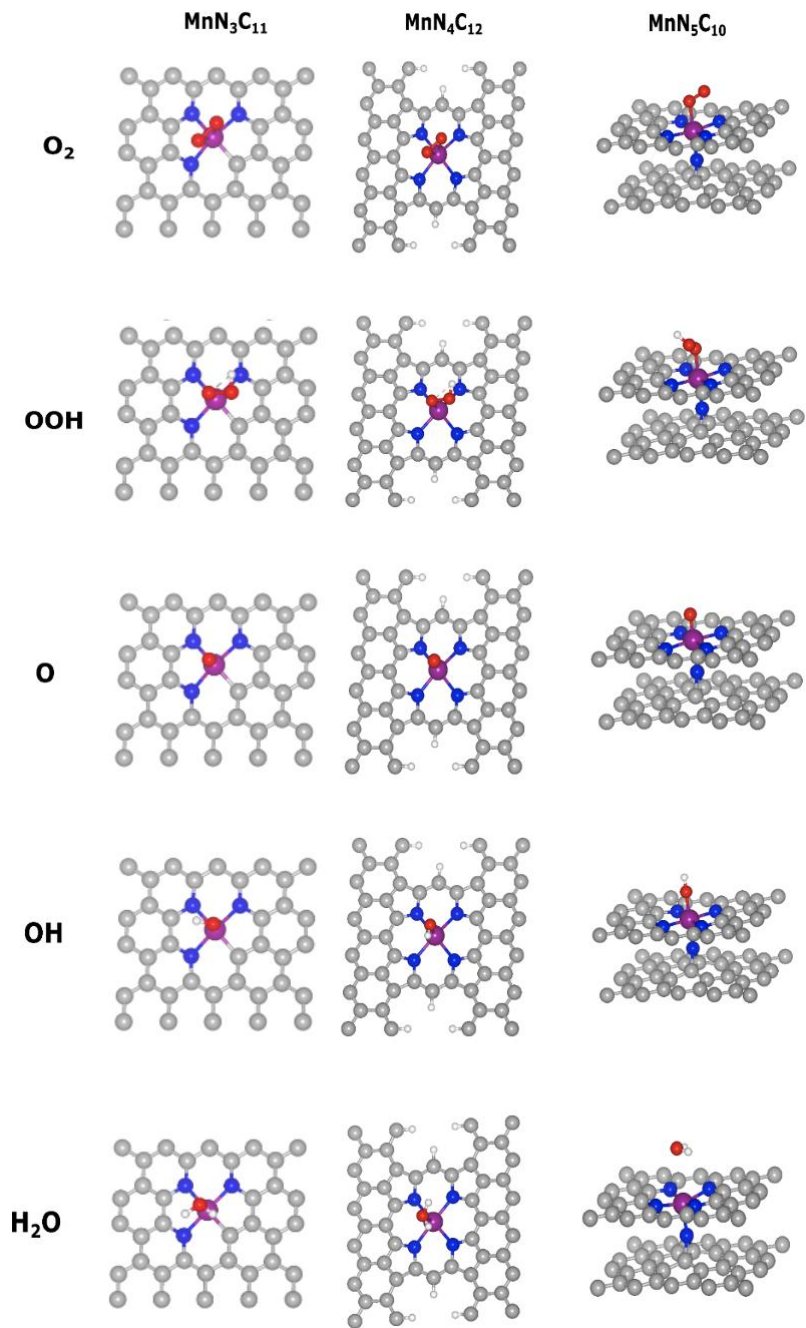
Figure 7.2 Atomistic structures of the optimized configurations of various ORR species adsorbed on the three MnN$_x$-types active sites. Column 1-3: MnN$_3$C$_{11}$, MnN$_4$C$_{12}$, and MnN$_5$C$_{10}$; Row 1-5: O$_2$, OOH, O, OH, and H$_2$O. In this figure, the gray, blue, purple, red, and white balls represent C, N, Mn, O, and H atoms, respectively.

Appendix A.3 Calculated Free Energy Evolution on Proposed MnNx Sites
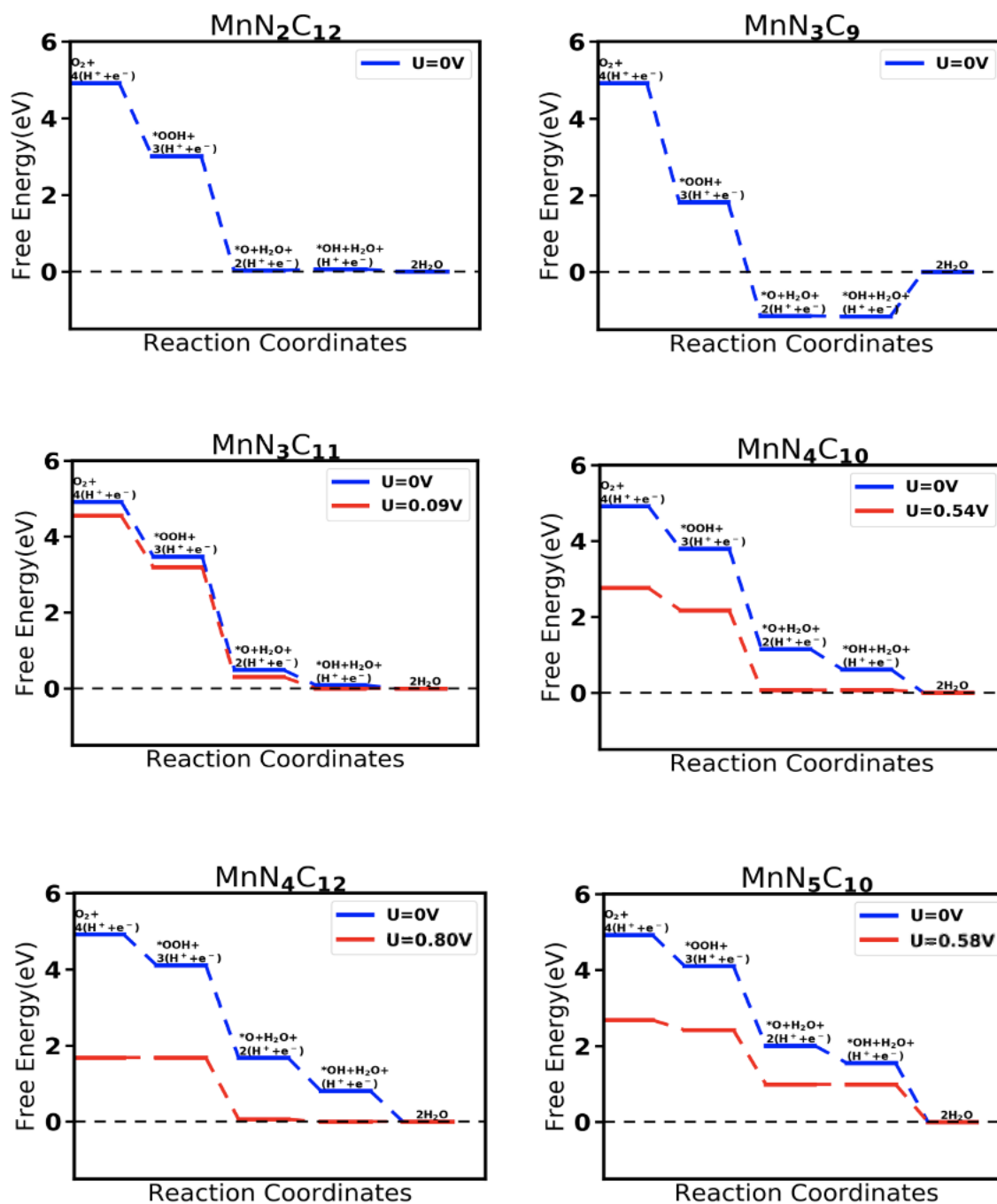
Figure 7.3 Calculated free energy evolution on proposed six MnNx sites

Bibliography

1   EIA, U., Energy Information Administration Monthly Energy Review. (2016).

2   Kirubakaran, A., Jain, S. & Nema, R. A review on fuel cell technologies and power electronic interface. *Renewable and Sustainable Energy Reviews* **13**, 2430-2440 (2009).

3   Farooque, M. & Maru, H. C. Fuel cells-the clean and efficient power generators. *Proceedings of the IEEE* **89**, 1819-1829, doi:10.1109/5.975917 (2001).

4   Stamenkovic, V. *et al.* Changing the activity of electrocatalysts for oxygen reduction by tuning the surface electronic structure. *Angewandte Chemie* **118**, 2963-2967 (2006).

5   Kongkanand, A. & Mathias, M. F. The priority and challenge of high-power performance of low-platinum proton-exchange membrane fuel cells. *The journal of physical chemistry letters* **7**, 1127-1137 (2016).

6   Oezaslan, M., Hasche, F. & Strasser, P. Pt-based core–shell catalyst architectures for oxygen fuel cell electrodes. *The Journal of Physical Chemistry Letters* **4**, 3273-3291 (2013).

7   Zeng, Y. *et al.* Regulating catalytic properties and thermal stability of Pt and PtCo intermetallic fuel-cell catalysts via strong coupling effects between single-metal site-rich carbon and Pt. *Journal of the American Chemical Society* **145**, 17643-17655 (2023).

8   Luo, M. & Guo, S. Strain-controlled electrocatalysis on multimetallic nanomaterials. *Nature Reviews Materials* **2**, 1-13 (2017).

9   Du, X. X., He, Y., Wang, X. X. & Wang, J. N. Fine-grained and fully ordered intermetallic PtFe catalysts with largely enhanced catalytic activity and durability. *Energ Environ Sci* **9**, 2623-2632 (2016).

10   Wang, X. X. *et al.* Ordered Pt3Co intermetallic nanoparticles derived from metal–organic frameworks for oxygen reduction. *Nano Lett* **18**, 4163-4171 (2018).

11   Chong, L. *et al.* Ultralow-loading platinum-cobalt fuel cell catalysts derived from imidazolate frameworks. *Science* **362**, 1276-1281 (2018).

12   Wang, X. X., Swihart, M. T. & Wu, G. Achievements, challenges and perspectives on cathode catalysts in proton exchange membrane fuel cells for transportation. *Nature Catalysis* **2**, 578-589 (2019).

13   Jasinski, R. A new fuel cell cathode catalyst. *Nature* **201**, 1212-1213 (1964).

14   Jahnke, H., Schönborn, M. & Zimmermann, G. Organic dyestuffs as catalysts for fuel cells. *Physical and chemical applications of dyestuffs*, 133-181 (1976).

15   Bezerra, C. W. *et al.* A review of heat-treatment effects on activity and stability of PEM fuel cell catalysts for oxygen reduction reaction. *J Power Sources* **173**, 891-908 (2007).

16   Van Veen, J. R., van Baar, J. F. & Kroese, K. J. Effect of heat treatment on the performance of carbon-supported transition-metal chelates in the electrochemical reduction of oxygen. *Journal of the Chemical Society, Faraday Transactions 1: Physical Chemistry in Condensed Phases* **77**, 2827-2843 (1981).

17   Sun, T., Tian, B., Lu, J. & Su, C. Recent advances in Fe (or Co)/N/C electrocatalysts for the oxygen reduction reaction in polymer electrolyte membrane fuel cells. *Journal of Materials Chemistry A* **5**, 18933-18950 (2017).

18   Qiao, Z. *et al.* 3D polymer hydrogel for high-performance atomic iron-rich catalysts for oxygen reduction in acidic media. *Applied Catalysis B: Environmental* **219**, 629-639 (2017).

19   Wu, G., More, K. L., Johnston, C. M. & Zelenay, P. High-performance electrocatalysts for oxygen reduction derived from polyaniline, iron, and cobalt. *Science* **332**, 443-447 (2011).

20   He, Y. *et al.* Highly active atomically dispersed CoN 4 fuel cell cathode catalysts derived from surfactant-assisted MOFs: carbon-shell confinement strategy. *Energy & Environmental Science* **12**, 250-260 (2019).

21   Li, J. *et al.* Atomically dispersed manganese catalysts for oxygen reduction in proton-exchange membrane fuel cells. *Nature Catalysis* **1**, 935-945 (2018).

22   Shao, Y., Dodelet, J. P., Wu, G. & Zelenay, P. PGM-free cathode catalysts for PEM fuel cells: a mini-review on stability challenges. *Advanced materials* **31**, 1807615 (2019).

23   Winterbourn, C. C. Toxicity of iron and hydrogen peroxide: the Fenton reaction. *Toxicology letters* **82**, 969-974 (1995).

24   Jung, E. *et al.* Atomic-level tuning of Co–N–C catalyst for high-performance electrochemical H2O2 production. *Nature materials* **19**, 436-442 (2020).

25   Hansen, H. A., Viswanathan, V. & Nørskov, J. K. Unifying kinetic and thermodynamic analysis of 2 e–and 4 e–reduction of oxygen on metal surfaces. *The Journal of Physical Chemistry C* **118**, 6706-6718 (2014).

26   Nørskov, J. K., Bligaard, T., Rossmeisl, J. & Christensen, C. H. Towards the computational design of solid catalysts. *Nature chemistry* **1**, 37-46 (2009).

27   Greeley, J. *et al.* Alloys of platinum and early transition metals as oxygen reduction electrocatalysts. *Nature chemistry* **1**, 552-556 (2009).

28   Varela, A. S. *et al.* Electrochemical reduction of CO2 on metal-nitrogen-doped carbon catalysts. *Acs Catalysis* **9**, 7270-7284 (2019).

29   Yeager, E. Dioxygen electrocatalysis: mechanisms in relation to catalyst structure. *J. Mol. Catal.;(Switzerland)* **38** (1986).

30   Wu, Z. Y. *et al.* Iron carbide nanoparticles encapsulated in mesoporous Fe-N-doped carbon nanofibers for efficient electrocatalysis. *Angewandte Chemie* **127**, 8297-8301 (2015).

31   Fu, X. *et al.* In situ polymer graphenization ingrained with nanoporosity in a nitrogenous electrocatalyst boosting the performance of polymer-electrolyte-membrane fuel cells. *Advanced Materials* **29**, 1604456 (2017).

32   Liang, H.-W., Wei, W., Wu, Z.-S., Feng, X. & Mullen, K. Mesoporous metal–nitrogen-doped carbon electrocatalysts for highly efficient oxygen reduction reaction. *J Am Chem Soc* **135**, 16002-16005 (2013).

33   Mamtani, K. *et al.* Evolution of N-coordinated iron–carbon (FeNC) catalysts and their oxygen reduction (ORR) performance in acidic media at various stages of catalyst synthesis: an attempt at benchmarking. *Catalysis Letters* **146**, 1749-1770 (2016).

34   Gong, K., Du, F., Xia, Z., Durstock, M. & Dai, L. Nitrogen-doped carbon nanotube arrays with high electrocatalytic activity for oxygen reduction. *Science* **323**, 760-764 (2009).

35   Xu, Z., Zhou, Z., Li, B., Wang, G. & Leu, P. W. Identification of efficient active sites in nitrogen-doped carbon nanotubes for oxygen reduction reaction. *The Journal of Physical Chemistry C* **124**, 8689-8696 (2020).

36   Chen, L.-F. *et al.* Synthesis of nitrogen-doped porous carbon nanofibers as an efficient electrode material for supercapacitors. *Acs Nano* **6**, 7092-7102 (2012).

37   Wu, Z.-Y. *et al.* Partially oxidized Ni nanoparticles supported on Ni-N co-doped carbon nanofibers as bifunctional electrocatalysts for overall water splitting. *Nano Energy* **51**, 286-293 (2018).

38   Liang, H.-W., Zhuang, X., Brüller, S., Feng, X. & Müllen, K. Hierarchically porous carbons with optimized nitrogen doping as highly active electrocatalysts for oxygen reduction. *Nature communications* **5**, 1-7 (2014).

39   Wang, Y. *et al.* CO electroreduction on single-atom copper. *Science Advances* **9**, eade3557 (2023).

40   Jiao, Y., Zheng, Y., Chen, P., Jaroniec, M. & Qiao, S.-Z. Molecular scaffolding strategy with synergistic active centers to facilitate electrocatalytic CO2 reduction to hydrocarbon/alcohol. *Journal of the American Chemical Society* **139**, 18093-18100 (2017).

41   Wu, G. & Zelenay, P. Nanostructured nonprecious metal catalysts for oxygen reduction reaction. *Accounts of chemical research* **46**, 1878-1889 (2013).

42   Lai, Q. *et al.* Metal–organic-framework-derived Fe-N/C electrocatalyst with five-coordinated Fe-N x sites for advanced oxygen reduction in acid media. *Acs Catal* **7**, 1655-1663 (2017).

43   Thomas, M. *et al.* Graphene oxide sheathed ZIF-8 microcrystals: engineered precursors of nitrogen-doped porous carbon for efficient oxygen reduction reaction (ORR) electrocatalysis. *ACS applied materials & interfaces* **8**, 29373-29382 (2016).

44   Zhong, H. x. *et al.* ZIF-8 derived graphene-based nitrogen-doped porous carbon sheets as highly efficient and durable oxygen reduction electrocatalysts. *Angewandte Chemie International Edition* **53**, 14235-14239 (2014).

45   Zhang, H. *et al.* Single atomic iron catalysts for oxygen reduction in acidic media: particle size control and thermal activation. *J Am Chem Soc* **139**, 14143-14149 (2017).

46   Liu, S. *et al.* Atomically dispersed iron sites with a nitrogen–carbon coating as highly active and durable oxygen reduction catalysts for fuel cells. *Nature Energy* **7**, 652-663 (2022).

47   Zhang, C. *et al.* Networking pyrolyzed zeolitic imidazolate frameworks by carbon nanotubes improves conductivity and enhances oxygen-reduction performance in polymer-electrolyte-membrane fuel cells. *Advanced Materials* **29**, 1604556 (2017).

48   Nallathambi, V., Lee, J.-W., Kumaraguru, S. P., Wu, G. & Popov, B. N. Development of high performance carbon composite catalyst for oxygen reduction reaction in PEM Proton Exchange Membrane fuel cells. *J Power Sources* **183**, 34-42 (2008).

49   Litster, S. Advanced PGM-free cathode engineering for high power density and durability. *US DOE 2018 Hydrogen and Fuel Cell Program AMR Proceedings* (2018).

50   Zeng, Y. *et al.* Tuning the thermal activation atmosphere breaks the activity–stability trade-off of Fe–N–C oxygen reduction fuel cell catalysts. *Nature Catalysis*, 1-13 (2023).

51   Wang, X. X. *et al.* Nitrogen-coordinated single cobalt atom catalysts for oxygen reduction in proton exchange membrane fuel cells. *Advanced Materials* **30**, 1706758 (2018).

52   Liu, K. *et al.* Mn-and N-doped carbon as promising catalysts for oxygen reduction reaction: Theoretical prediction and experimental validation. *Applied Catalysis B: Environmental* **243**, 195-203 (2019).

53   Najam, T., Shah, S. S. A., Ding, W. & Wei, Z. Role of P-doping in antipoisoning: efficient MOF-derived 3D hierarchical architectures for the oxygen reduction reaction. *The journal of physical chemistry C* **123**, 16796-16803 (2019).

54   Guo, L. *et al.* Promoting Atomically Dispersed MnN4 Sites via Sulfur Doping for Oxygen Reduction: Unveiling Intrinsic Activity and Degradation in Fuel Cells. *Acs Nano* **15**, 6886-6899 (2021).

55   Yuan, K. *et al.* Synergetic contribution of boron and Fe–N x species in porous carbons toward efficient electrocatalysts for oxygen reduction reaction. *ACS Energy Letters* **3**, 252-260 (2017).

56   Holby, E. F., Wu, G., Zelenay, P. & Taylor, C. D. Structure of Fe–N x–C Defects in Oxygen Reduction Reaction Catalysts from First-Principles Modeling. *The Journal of Physical Chemistry C* **118**, 14388-14393 (2014).

57   Lefèvre, M., Proietti, E., Jaouen, F. & Dodelet, J.-P. Iron-based catalysts with improved oxygen reduction activity in polymer electrolyte fuel cells. *Science* **324**, 71-74 (2009).

58   Charreteur, F., Jaouen, F., Ruggeri, S. & Dodelet, J.-P. Fe/N/C non-precious catalysts for PEM fuel cells: Influence of the structural parameters of pristine commercial carbon blacks on their activity for oxygen reduction. *Electrochim Acta* **53**, 2925-2938 (2008).

59   Deng, D. *et al.* A single iron site confined in a graphene matrix for the catalytic oxidation of benzene at room temperature. *Science advances* **1**, e1500462 (2015).

60   Li, Q. *et al.* Phosphate-tolerant oxygen reduction catalysts. *Acs Catal* **4**, 3193-3200 (2014).

61   Ferrandon, M. *et al.* Multitechnique Characterization of a Polyaniline–Iron–Carbon Oxygen Reduction Catalyst. *The Journal of Physical Chemistry C* **116**, 16001-16013, doi:10.1021/jp302396g (2012).

62   Zitolo, A. *et al.* Identification of catalytic sites for oxygen reduction in iron-and nitrogen-doped graphene materials. *Nature materials* **14**, 937-942 (2015).

63   Wan, X. *et al.* Fe–N–C electrocatalyst with dense active sites and efficient mass transport for high-performance proton exchange membrane fuel cells. *Nature Catalysis* **2**, 259-268 (2019).

64   Pan, F. *et al.* N and OH-Immobilized Cu3 Clusters In Situ Reconstructed from Single-Metal Sites for Efficient CO2 Electromethanation in Bicontinuous Mesochannels. *Journal of the American Chemical Society* (2024).

65   Li, J. *et al.* Identification of durable and non-durable FeN x sites in Fe–N–C materials for proton exchange membrane fuel cells. *Nature Catalysis* **4**, 10-19 (2021).

66   Mineva, T. *et al.* Understanding active sites in pyrolyzed Fe–N–C catalysts for fuel cell cathodes by bridging density functional theory calculations and 57Fe Mossbauer spectroscopy. *ACS Catalysis* **9**, 9359-9371 (2019).

67   Chenitz, R. *et al.* A specific demetalation of Fe–N 4 catalytic sites in the micropores of NC_Ar+ NH 3 is at the origin of the initial activity loss of the highly active Fe/N/C catalyst used for the reduction of oxygen in PEM fuel cells. *Energ Environ Sci* **11**, 365-382 (2018).

68   Choi, C. H. *et al.* Stability of Fe-N-C catalysts in acidic medium studied by operando spectroscopy. *Angewandte Chemie International Edition* **54**, 12753-12757 (2015).

69   Choi, C. H. *et al.* Minimizing operando demetallation of Fe-NC electrocatalysts in acidic medium. *Acs Catal* **6**, 3136-3146 (2016).

70   Yuan, X.-Z., Li, H., Zhang, S., Martin, J. & Wang, H. A review of polymer electrolyte membrane fuel cell durability test protocols. *J Power Sources* **196**, 9107-9116 (2011).

71   Aikens, D.   (ACS Publications, 1983).

72   Norskov, J. K. *et al.* Origin of the overpotential for oxygen reduction at a fuel-cell cathode. *Journal of Physical Chemistry B* **108**, 17886-17892, doi:10.1021/jp047349j (2004).

73   Hansen, H. A., Rossmeisl, J. & Nørskov, J. K. Surface Pourbaix diagrams and oxygen reduction activity of Pt, Ag and Ni (111) surfaces studied by DFT. *Phys Chem Chem Phys* **10**, 3722-3730 (2008).

74   Siahrostami, S. *et al.* Enabling direct H 2 O 2 production through rational electrocatalyst design. *Nature materials* **12**, 1137-1143 (2013).

75   Kulkarni, A., Siahrostami, S., Patel, A. & Nørskov, J. K. Understanding catalytic activity trends in the oxygen reduction reaction. *Chemical Reviews* **118**, 2302-2312 (2018).

76   Vassilev, P. & Koper, M. T. Electrochemical reduction of oxygen on gold surfaces: a density functional theory study of intermediates and reaction paths. *The Journal of Physical Chemistry C* **111**, 2607-2613 (2007).

77   Zhong, G. *et al.* Green synthesis of iron and nitrogen co-doped porous carbon via pyrolysing lotus root as a high-performance electrocatalyst for oxygen reduction reaction. *International Journal of Energy Research* **45**, 10393-10408 (2021).

78   Liu, K., Wu, G. & Wang, G. Role of Local Carbon Structure Surrounding FeN4 Sites in Boosting the Catalytic Activity for Oxygen Reduction. *The Journal of Physical Chemistry C* **121**, 11319-11324, doi:10.1021/acs.jpcc.7b00913 (2017).

79   Xu, H., Cheng, D., Cao, D. & Zeng, X. C. A universal principle for a rational design of single-atom electrocatalysts. *Nature Catalysis* **1**, 339-348, doi:10.1038/s41929-018-0063-z (2018).

80   Liu, K., Kattel, S., Mao, V. & Wang, G. Electrochemical and computational study of oxygen reduction reaction on nonprecious transition metal/nitrogen doped carbon nanofibers in acid medium. *The Journal of Physical Chemistry C* **120**, 1586-1596 (2016).

81   Zhao, X. & Liu, Y. Origin of Selective Production of Hydrogen Peroxide by Electrochemical Oxygen Reduction. *Journal of the American Chemical Society* **143**, 9423-9428, doi:10.1021/jacs.1c02186 (2021).

82   Wang, Y., Tang, Y.-J. & Zhou, K. Self-adjusting activity induced by intrinsic reaction intermediate in Fe–N–C single-atom catalysts. *J Am Chem Soc* **141**, 14115-14119 (2019).

83   Hohenberg, P. & Kohn, W. Inhomogeneous Electron Gas. *Physical Review B* **136**, B864-+ (1964).

84   Kohn, W. & Sham, L. J. Self-Consistent Equations Including Exchange and Correlation Effects. *Physical Review* **140**, 1133-& (1965).

85   Seh, Z. W. *et al.* Combining theory and experiment in electrocatalysis: Insights into materials design. *Science* **355**, eaad4998 (2017).

86   Zhao, X., Levell, Z. H., Yu, S. & Liu, Y. Atomistic understanding of two-dimensional electrocatalysts from first principles. *Chemical Reviews* **122**, 10675-10709 (2022).

87   Greeley, J. *et al.* Alloys of platinum and early transition metals as oxygen reduction electrocatalysts. *Nature Chemistry* **1**, 552-556, doi:10.1038/nchem.367 (2009).

88   Kresse, G. & Furthmuller, J. Efficiency of ab-initio total energy calculations for metals and semiconductors using a plane-wave basis set. *Computational Materials Science* **6**, 15-50 (1996).

89   Kresse, G. & Hafner, J. Ab initiomolecular dynamics for liquid metals. *Phys Rev B* **47**, 558-561, doi:10.1103/physrevb.47.558 (1993).

90   Blochl, P. E. Projector Augmented-Wave Method. *Physical Review B* **50**, 17953-17979 (1994).

91   Kresse, G. & Joubert, D. From ultrasoft pseudopotentials to the projector augmented-wave method. *Physical Review B* **59**, 1758-1775 (1999).

92   Perdew, J. P., Burke, K. & Ernzerhof, M. Generalized gradient approximation made simple. *Physical Review Letters* **77**, 3865-3868 (1996).

93   Monkhorst, H. J. & Pack, J. D. Special Points for Brillouin-Zone Integrations. *Physical Review B* **13**, 5188-5192 (1976).

94   Henkelman, G., Uberuaga, B. P. & Jonsson, H. A climbing image nudged elastic band method for finding saddle points and minimum energy paths. *J Chem Phys* **113**, 9901-9904 (2000).

95   Yang, J. *et al.* Compressive strain modulation of single iron sites on helical carbon support boosts electrocatalytic oxygen reduction. *Angewandte Chemie International Edition* **60**, 22722-22728 (2021).

96   Zhong, W. *et al.* Identifying the active sites of a single atom catalyst with pH-universal oxygen reduction reaction activity. *Cell Reports Physical Science* **1** (2020).

97   Rossmeisl, J., Nørskov, J. K., Taylor, C. D., Janik, M. J. & Neurock, M. Calculated phase diagrams for the electrochemical oxidation and reduction of water over Pt (111). *The Journal of Physical Chemistry B* **110**, 21833-21839 (2006).

98   Duan, Z. & Henkelman, G. Theoretical resolution of the exceptional oxygen reduction activity of Au (100) in alkaline media. *Acs Catal* **9**, 5567-5573 (2019).

99   Gauthier, J. A. *et al.* Unified approach to implicit and explicit solvent simulations of electrochemical reaction energetics. *Journal of chemical theory and computation* **15**, 6895-6906 (2019).

100   Gauthier, J. A., Dickens, C. F., Ringe, S. & Chan, K. Practical considerations for continuum models applied to surface electrochemistry. *ChemPhysChem* **20**, 3074-3080 (2019).

101   Nørskov, J. K., Studt, F., Abild-Pedersen, F. & Bligaard, T. *Fundamental concepts in heterogeneous catalysis*. (John Wiley & Sons, 2014).

102   Mehmood, A. *et al.* High loading of single atomic iron sites in Fe–NC oxygen reduction catalysts for proton exchange membrane fuel cells. *Nature Catalysis* **5**, 311-323, doi:10.1038/s41929-022-00772-9 (2022).

103   Gómez-Marín, A. M. & Feliu, J. M. New insights into the oxygen reduction reaction mechanism on Pt (111): A detailed electrochemical study. *ChemSusChem* **6**, 1091-1100 (2013).

104   Sha, Y., Yu, T. H., Merinov, B. V., Shirvanian, P. & Goddard, W. A. Mechanism for Oxygen Reduction Reaction on Pt3Ni Alloy Fuel Cell Cathode. *The Journal of Physical Chemistry C* **116**, 21334-21342, doi:10.1021/jp303966u (2012).

105   Stracensky, T. *et al.* Bypassing Formation of Oxide Intermediate via Chemical Vapor Deposition for the Synthesis of an Mn-NC Catalyst with Improved ORR Activity. *ACS catalysis* **13**, 14782-14791 (2023).

106   Cottrell, T. L. *The strengths of chemical bonds*. (Butterworths Scientific Publications, 1958).

107   Li, J. *et al.* Identification of durable and non-durable FeNx sites in Fe–N–C materials for proton exchange membrane fuel cells. *Nature Catalysis* **4**, 10-19, doi:10.1038/s41929-020-00545-2 (2021).

108   Liu, K., Lei, Y. & Wang, G. Correlation between oxygen adsorption energy and electronic structure of transition metal macrocyclic complexes. *J Chem Phys* **139**, 204306, doi:10.1063/1.4832696 (2013).

109   Sanville, E., Kenny, S. D., Smith, R. & Henkelman, G. Improved grid-based algorithm for Bader charge allocation. *Journal of computational chemistry* **28**, 899-908 (2007).

110   Wu, Z. Y. *et al.* Iron carbide nanoparticles encapsulated in mesoporous Fe-N-doped carbon nanofibers for efficient electrocatalysis. *Angewandte Chemie International Edition* **54**, 8179-8183 (2015).

111.   Liu, K. X. *et al.* Mn- and N- doped carbon as promising catalysts for oxygenb reduction reaction: Theoretical prediction and experimental validation. *Applied Catalysis B: Environemnt* **243**, 195-203 (2019)

112   Banham, D. *et al.* A review of the stability and durability of non-precious metal catalysts for the oxygen reduction reaction in proton exchange membrane fuel cells. *J. Power Sources* **285**, 334-348 (2015).

113   Kattel, S. & Wang, G. Reaction Pathway for Oxygen Reduction on FeN_4 Embedded Graphene. *The Journal of Physical Chemistry Letters* **5**, 452-456, doi:10.1021/jz402717r (2014).

114   Martinez, U., Komini Babu, S., Holby, E. F. & Zelenay, P. Durability challenges and perspective in the development of PGM-free electrocatalysts for the oxygen reduction reaction. *Current Opinion in Electrochemistry* **9**, 224-232, (2018).

115   Luo, J.-H., Hong, Z.-S., Chao, T.-H. & Cheng, M.-J. Quantum mechanical screening of metal-N4-functionalized graphenes for electrochemical anodic oxidation of light alkanes to oxygenates. *The Journal of Physical Chemistry C* **123**, 19033-19044 (2019).

116   Wang, H., Zhang, L., Han, J. & Weinan, E. DeePMD-kit: A deep learning package for many-body potential energy representation and molecular dynamics. *Computer Physics Communications* **228**, 178-184 (2018).

117   Chanussot, L. *et al.* Open catalyst 2020 (OC20) dataset and community challenges. *Acs Catalysis* **11**, 6059-6072 (2021).